Intelligent optimization of particle size distribution in unscreened recycled coarse aggregates using 3D surface analysis

Chang, Cheng; Maio, Francesco Di; Bheemireddy, Rajeev; Posthoorn, Perry; Gebremariam, Abraham T.; Rem, Peter

DOI
10.1016/j.jii.2025.100864

Publication date
2025

Document Version
Final published version

Published in
Journal of Industrial Information Integration

Journal of Industrial Information Integration 46 (2025) 100864

Contents lists available at ScienceDirect

Journal of Industrial Information Integration

journal homepage: www.sciencedirect.com/journal/journal-of-industrial-information-integration

Full Length Article

Intelligent optimization of particle size distribution in unscreened recycled coarse aggregates using 3D surface analysis

Cheng Chang [a,*], Francesco Di Maio [a], Rajeev Bheemireddy [b], Perry Posthoorn [b], Abraham T. Gebremariam [a], Peter Rem [a]

[a] Resource & Recycling, Department of Engineering Structures, Faculty of Civil Engineering and Geosciences, Delft University of Technology, Stevinweg 1, 2628 CN, Delft, the Netherlands

[b] DEMO, Delft University of Technology, Gebouw 36, Mekelweg 4, 2628 CD, Delft, the Netherlands

ARTICLE INFO

Keywords:
Recycled coarse aggregates
Particle size distribution
3D surface analysis
Quality assurance
Concrete recycling
Non-contact measurement

ABSTRACT

The efficient measurement and optimization of the particle size distribution (PSD) of recycled coarse aggregates (RCA) is critical to ensuring consistent quality in high-performance concrete production. Unlike primary aggregates, which typically demonstrate minimal variability over extended periods and require only occasional testing, RCA often exhibit substantial fluctuations in quality over short timeframes. This variability necessitates a precise, automated, and real-time quality assessment approach, which is lacking in conventional aggregate processing. In this study, a rapid, automated, and non-contact 3D surface analysis method is proposed to assess and optimize the PSD of unscreened RCA during continuous transport on a conveyor belt. A custom-designed conical feeder and splitter facilitate the formation of continuous, symmetric triangular RCA piles, ranging from 4.0 to 16.0 mm in size. Representative PSD measurements are obtained by analyzing a designated strip located at one-third of the pile's height. High-resolution 3D point cloud data are processed using a watershed segmentation algorithm that leverages gradient-based path tracing for efficient topographical mapping. This enables parallel data processing, thereby reducing computational time. The proposed method enables real-time and accurate PSD analysis at industrial throughput levels (≥50 tons per hour) without interrupting conveyor operation, achieving a Root Mean Square Error (RMSE) between 4.69 % and 6.09 %. Furthermore, an optimization strategy based on cumulative percentage retained curves enhances RCA quality and supports continuous process control. The integration of these techniques contributes to improved RCA management and promotes sustainable resource utilization and waste reduction in the construction sector.

List of acronyms

Acronym	Meaning
ADR	Advanced Dry Recovery
C2CA	Concrete to Cement and Aggregate
PSD	Particle Size Distribution
RCA	Recycled Coarse Aggregates
RMSE	Root Mean Square Error

1. Introduction

Recycled coarse aggregates (RCA), derived from demolition waste, have gained increasing attention in sustainable construction due to their potential to reduce environmental impact and conserve natural resources. However, a key challenge hindering their widespread application is the frequent and substantial variability in quality [1]. Unlike primary aggregates, which are sourced from consistent geological formations and thus maintain stable quality over extended periods, RCA can exhibit significant quality fluctuations over short timeframes, often as brief as a single truckload. This inconsistency is primarily attributable to the heterogeneous composition of demolition waste—originating from various structural components and demolition sites—and differences in recycling processes. Consequently, fluctuations in the composition and properties of the incoming demolition waste directly affect the consistency of the produced RCA [2,3].

This inconsistency significantly impedes compliance with the stringent specifications required for high-performance concrete applications. While RCA holds environmental advantages, its unpredictable quality

* Corresponding author.
E-mail addresses: chang-cheng@outlook.com, C.Chang-1@tudelft.nl (C. Chang).

https://doi.org/10.1016/j.jii.2025.100864

Available online 12 May 2025

limits its reliability in critical structural contexts. Construction projects often have precise requirements for aggregate quality to ensure the safety and longevity of structures [4]. Consequently, more frequent and rigorous testing is required, which increases both operational complexity and cost [5,6]. Moreover, variable input quality complicates process optimization in recycling facilities, particularly in sorting and classification operations, leading to inefficiencies, equipment wear, and potentially the need for batch reprocessing [7].

The motivation of this study arises from the increasing importance of RCA in sustainable construction practices, driven by global sustainability goals and resource efficiency requirements. There is a growing industrial demand for consistent RCA quality to reliably produce high-performance concrete. However, RCA typically exhibits considerable variability due to the heterogeneous nature of demolition waste, posing significant challenges in consistently meeting stringent specifications for concrete applications. Traditional quality assessment methods, primarily manual sampling and laboratory testing, suffer from substantial limitations including high operational costs, susceptibility to human errors, and inability to provide real-time feedback for immediate process adjustments. Additionally, current automated systems relying on conventional 2D imaging methods are often inadequate due to their limited accuracy when analyzing dense, overlapping, and irregularly shaped RCA particles under dynamic, industrial-scale conditions.

To address these challenges, this study introduces an innovative automated solution integrating advanced 3D surface analysis technology with intelligent particle size distribution (PSD) optimization methods. Specifically, the key contributions of this research include: (1) the design and implementation of a novel conical feeder and splitter system that ensures representative and stable formation of RCA piles on conveyor belts, enabling accurate and consistent surface measurements; (2) the development of a robust and optimized watershed segmentation algorithm tailored specifically for processing high-resolution 3D point cloud data, effectively overcoming technical limitations related to particle overlap, irregular shapes, and dense particle distributions; and (3) the integration of a minimal-adjustment PSD correction optimization technique, facilitating real-time optimization and significantly improving RCA quality control. Collectively, these contributions enable substantial advancements in automated real-time RCA quality assessment, reduce operational costs, enhance process efficiency, and support sustainable, high-quality concrete production at an industrial scale.

Fig. 1 illustrates the procedural flowchart, offering a visual summary of the methodological sequence employed in this study.

This work contributes to the field in several novel ways. First, it introduces a fully automated, non-contact 3D scanning system capable of real-time PSD assessment for unscreened RCA in motion on a high-speed conveyor—an operational context rarely addressed in existing studies. Second, the proposed watershed-based segmentation algorithm is tailored to the morphological complexity of RCA piles, allowing robust delineation of overlapping and irregular particles, which conventional image-based or static 3D methods often fail to resolve. Third, by integrating linear programming with cumulative percentage retained curves from European standards, the method enables intelligent, in-line PSD optimization—establishing a practical closed-loop system for industrial quality control. Together, these innovations fill a critical gap between laboratory-scale particle analysis and industrial-scale RCA management.

This study makes a substantive contribution to the field of industrial information integration by proposing a digital, real-time, and closed-loop system for the monitoring and optimization of RCA quality. With the construction sector increasingly adopting recycled materials to meet sustainability goals, there is a pressing need for advanced, data-driven quality assurance and control methods. By embedding non-contact 3D surface analysis and high-resolution point cloud processing within the RCA recycling workflow, the proposed system enables continuous and accurate assessment of PSD. Furthermore, the incorporation of intelligent PSD correction using linear programming establishes a feedback-oriented control mechanism that mirrors a cyber-physical system architecture. This approach effectively bridges the gap between material-level sensing and large-scale process management. The methodology presented not only supports real-time decision-making and process optimization but also aligns with broader industrial trends toward digital twin frameworks, smart manufacturing, and the integration of sustainable technologies in production environments—cornerstones of modern industrial information integration.

The remainder of this paper is organized as follows: Section 2 presents a comprehensive literature review of PSD assessment methods and challenges in RCA quality control. Section 3 details the materials used, the experimental setup, the design of the 3D scanning and analysis system, and the PSD optimization method based on cumulative percentage retained curves and linear programming. Section 4 discusses the results, including sampling representativeness, point cloud

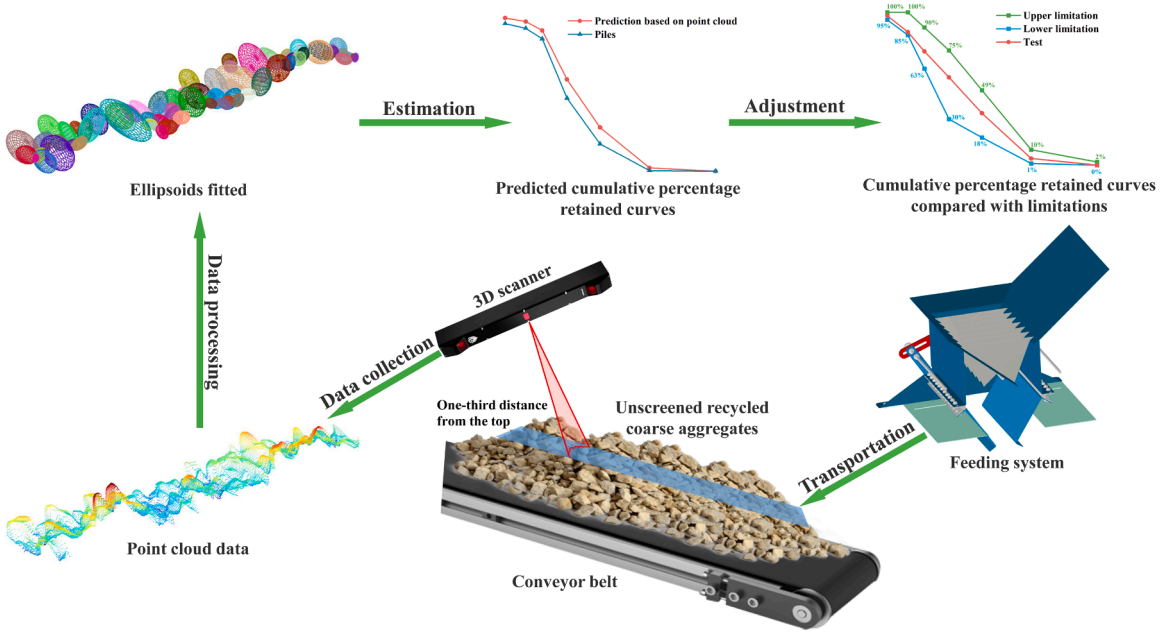

Fig. 1. Schematic of industrial-scale implementation for intelligent PSD optimization.

segmentation accuracy, PSD estimation performance, and the effects of PSD adjustment. Finally, Section 5 concludes the study, highlights key findings, and proposes directions for future research.

2. Literature review

The assessment of RCA presents considerable challenges in terms of accuracy, efficiency, and real-time monitoring. Extensive research [8–14] has been conducted in this area to address these challenges. Among various physical properties, PSD plays a critical role in determining the workability, strength, and durability of the resulting concrete [15–18]. An imbalance in PSD—whether skewed towards fine or coarse fractions—can adversely affect mixture cohesiveness, leading to reduced structural performance. Therefore, precise PSD characterization is essential, especially in large-scale production contexts where process reliability is paramount.

Traditionally, PSD has been evaluated through manual sampling and laboratory-based sieving methods [19,20]. While widely used, these approaches are labor-intensive, asynchronous, and prone to operator error [21]. Such methods cannot provide timely feedback to the operator of the recycling plant, essential for detecting off-spec production and ensuring stable and guaranteed quality to facilities [22]. The practice of sampling the plant stream, conducting sieving tests in the laboratory, and then incorporating the results back into the plant control system often introduces a significant lag time. This lag time can delay decision-making processes and hinder the optimization of recycling operations [23]. The use of online automated non-contact measurement techniques [24] for real-time PSD analysis can help mitigate this issue by providing immediate feedback on the PSD, enabling timely adjustments and optimization of the recycling process. Online automated PSD measurement delivers a digital result, and so it is an essential component of digital recycling plants, which offer a further cost reduction for sustainable concrete production.

Over the past few decades, the use of image-based PSD analysis has gained significant attention due to the progress in computer vision and digital image processing [25–30]. However, conventional image-based [31,32] systems used for PSD analysis have several limitations that need to be addressed. One significant limitation is the susceptibility of these systems to surrounding conditions [33,34]. The properties of the material surfaces being analyzed also pose challenges [35,36]. Different materials may reflect or absorb light differently, leading to variations in the captured images. Acquiring information about particles located beneath the surface is another obstacle in traditional imaging techniques [37,38]. Additionally, distinguishing between superimposed and non-superimposed particles presents a challenge in image-based PSD analysis [37,39]. Errors in PSD analysis mainly stem from the analysis methods or algorithms employed [40–43]. If these methods are not properly validated or optimized, they can contribute to errors such as over-segmentation and under-segmentation [44,45].

In recent years, with the informatization and digitalization of the construction industry [46–50] facilitated digitally driven processes and integrated functional digital twins [51–56], advancements in 3D scanning technology have revolutionized the field of object measurement [57–60]. This technology enables the capturing of detailed geometric information of aggregate piles on conveyor belts, effectively overcoming challenges related to color or illumination variations [61]. However, the application of 3D scanners for PSD analysis of aggregate piles on conveyor belts presents unique challenges. One such challenge is the high-speed movement of the material on the conveyor belts. As the aggregate piles are transported rapidly, the particles should move as little as possible and the 3D scanner must capture precise measurements within a short period. This necessitates the development of robust transportation methods, efficient scanning techniques, and hardware capable of acquiring accurate data in real time. Moreover, handling the large volume of data generated by the 3D scanner presents a data processing challenge. To achieve real-time analysis, sophisticated algorithms are required to efficiently process and analyze the acquired data [62]. These algorithms should be capable of handling the high data throughput and extracting meaningful information about the PSD from the scanned data. Another challenge is the presence of segregation and grouping errors [61], which refers to the tendency of larger particles to rise to the surface of the pile, while smaller particles tend to settle at the bottom. This uneven distribution can introduce errors in the PSD analysis. Currently, the analysis of particle piles on conveyor belts has received less attention in the literature compared to single-layer particle analysis [44,63]. Nonetheless, ongoing research is being conducted to address these challenges and explore new methodologies for analyzing particle piles on conveyor belts. Table 1 summarizes key studies relevant to PSD analysis, highlighting their methodologies, findings, and how they inform the current study. By developing innovative approaches and algorithms, researchers aim to improve the accuracy and efficiency of PSD analysis using 3D scanning technology.

Recent advancements in industrial information integration have underscored the transformative potential of integrating intelligent sensing and data analytics for real-time process control [64,65]. For instance, Mishra et al. [66] proposed a computer vision-based framework that integrates Swin Transformer and U-Net architectures to detect material inclusions in industrial environments, showcasing the effectiveness in defect recognition. Mazzoleni [67] emphasized a data-driven approach to industrial supervision, outlining a design methodology centered on experimental data acquisition and failure reproduction to improve system reliability. Ali et al. [68] introduced a machine learning-based integration technique designed to address the complexities of monitoring physical and industrial processes under real-world operational constraints. Borhani et al. [69] conducted a comprehensive review of the architecture, capabilities, and limitations of various industrial scanning devices, particularly within Supervisory Control and Data Acquisition systems used for infrastructure monitoring and control. Chang et al. [12,13] demonstrated the potential of combining Laser-Induced Breakdown Spectroscopy with 3D scanning for rapid contaminant detection, thereby validating the applicability of multi-sensor fusion in automated quality assurance. Singh et al. [70] developed a Smart Machine Monitoring System that integrates IoT infrastructure with artificial intelligence algorithms to enhance utilization of computer numerical control and special-purpose machines, enabling adaptive scheduling and real-time diagnostics. Building on these prior innovations, the present study introduces a novel, high-throughput, and fully automated framework for PSD analysis and optimization tailored to unscreened RCA. This work addresses a critical gap in the current literature by extending industrial sensing and intelligent decision-making into a domain that remains largely overlooked. Through the integration of non-contact 3D surface scanning, high-resolution point cloud processing, and PSD correction via linear programming, the proposed system embodies key tenets of industrial information integration. It effectively links material-level quality sensing with industrial-scale process control, thereby contributing to the advancement of intelligent manufacturing and sustainable construction practices.

In summary, the current body of research emphasizes the need for robust, real-time, and high-resolution PSD assessment systems tailored to the inherent variability of RCA and the constraints of industrial recycling processes. While 2D image-based systems provide a partial solution, their limitations in dense and dynamic settings remain unresolved. This study addresses this critical gap by introducing a real-time 3D scanning framework specifically designed for unscreened RCA on conveyor belts. By combining accurate surface analysis with intelligent PSD optimization, the proposed method achieves higher precision and process adaptability than conventional techniques.

3. Materials and methods

This section presents the materials, experimental setup, and methods

Table 1
Comparative analysis of related studies for PSD.

Study	Methodology	Application area	Real-time	High throughput	Dynamic environment	Automated	Optimization applied
Shrivastava et al. [31]	2D image + convolutional neural networks	Dump materials	✓	×	×	×	×
Yang et al. [32]	2D image + digital imaging processing	Coal fragments	×	×	×	×	×
Tafesse et al. [33]	2D image + 3D image analysis	Coarse particles	×	×	×	×	×
Bai et al. [36]	2D image + digital imaging processing	Coal particles	✓	×	×	×	×
Hamzeloo et al. [37]	2D image + image processing and neural network	Crushing circuit	✓	×	×	×	×
Wu et al. [38]	2D image + digital imaging processing	Iron green pellets	✓	×	✓	✓	×
Olivier et al. [43]	2D image + deep convolutional neural networks	Ore particles	×	×	×	×	×
Engin et al. [44]	3D scanning + point cloud data processing	Grains	×	×	×	×	×
Zhang et al. [45]	2D image + digital imaging processing	Coal particles	✓	×	✓	✓	×
Current study	3D scanning + point cloud data processing	RCA	✓	✓	✓	✓	✓

Note: ✓ indicates the feature is present in the referenced study; × indicates it is not addressed.

employed to assess and optimize the PSD of unscreened RCA using a real-time 3D surface analysis system. The section is structured as follows: Section 3.1 describes the origin and properties of the RCA materials used in this study. Sections 3.2 introduce the specially designed feeding system and the 3D scanning setup used to generate triangular RCA piles and capture surface geometry data. Section 3.3 explains the sampling strategy for selecting representative areas on the pile surface. Section 3.4 provides a detailed explanation of the 3D point cloud processing and segmentation algorithms, also presents the PSD optimization strategy based on linear programming. Together, these methods form an integrated system for the intelligent analysis and adjustment of the PSD of RCA in industrial settings.

3.1. Materials

RCA used in this study were produced using the Concrete to Cement and Aggregate (C2CA) technology, which was applied to batches of end-of-life concrete obtained from dismantled construction sites across various locations in The Netherlands [71]. This sampling approach incorporated a range of material characteristics, enabling an investigation into the influence of source variability on PSD and overall RCA quality.

The collected material was processed through a sequence of mechanical treatments defined within the C2CA framework. Specifically, particles in the 0–16.0 mm range were treated using the Advanced Dry Recovery (ADR) technique [71]. This process resulted in two main output fractions: RCA with particle sizes between 4.0 and 16.0 mm, and a fine fraction (0–4.0 mm), which was separated as a distinct by-product for potential secondary applications.

3.2. Equipment

3.2.1. Feeding system

The feeding system of the 3D scanning setup (Fig. 2) comprises two primary components: a conical feeder and a splitter. Its function is to ensure a continuous, controlled flow of RCA and to form stable, symmetric triangular piles on the conveyor belt for subsequent analysis.

RCA are introduced at the top section of the conical feeder, which

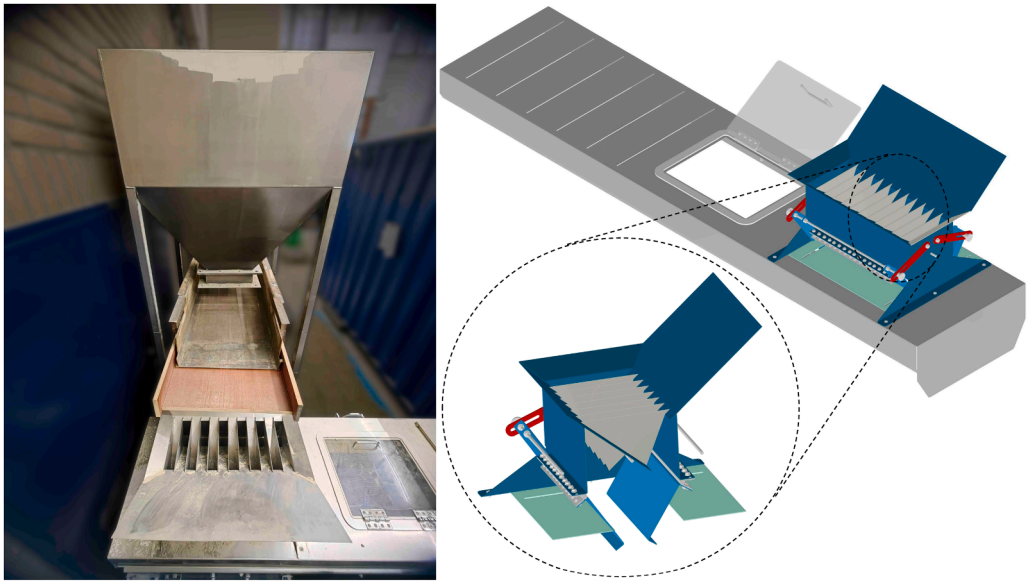

(a) Conical feeder and splitter *(b) Cross-sectional view of the splitter*

Fig. 2. Feeding system.

regulates the initial flow. The material is then transferred into the splitter under vibration-induced motion. The vibration frequency was maintained at 30 Hz, with the amplitude controlled by adjusting the input voltage through a dedicated controller.

The splitter plays a critical role in evenly distributing the incoming RCA. It is equipped with two sets of symmetrically positioned triangular slots specifically designed to divide the material stream into two equal parts. As RCA enter the splitter (Fig. 3), particles follow varied paths—some fall directly, while others reflect off the internal surfaces—before passing through the bottom outlet and depositing onto the conveyor belt.

This process is designed to achieve symmetrical distribution of RCA particles across each layer—and by extension, each half-layer—of the triangular piles formed on the conveyor belt (Fig. 4). The geometry of the conical feeder and the symmetric configuration of the splitter are intended to provide each particle type with an equal probability of being distributed uniformly along the feeder's perimeter. As a result, the deposited pile is expected to maintain uniform particle distribution within half-layers of consistent thickness, formed at a continuous critical slope.

Nonetheless, subsequent experimental observations revealed that the actual PSD and material composition are not entirely uniform across the pile. Variations persist along the pile slope, indicating that perfect uniformity is not fully achieved despite the symmetric feeding design.

After a series of controlled experiments, it was determined that at a conveyor belt speed of 0.529 m/s, the resulting triangular piles exhibited a base width of 37 cm and a height of 9 $\pm$ 0.5 cm. Based on this configuration, the system is capable of processing at least 50 tons of RCA per hour. The geometric stability and uniformity of these triangular piles are critical for accurate PSD assessment, as they ensure consistent spatial representation of particle distribution. The feeding system plays a central role in achieving this, enabling controlled RCA delivery and supporting reliable surface-based PSD analysis.

The consistent formation of stable triangular piles can be attributed to a combination of material properties and system design parameters:

(1) Particle morphology: RCA particles exhibit irregular, angular geometries—often featuring convex and concave surfaces—that promote interlocking and stable pile formation. Compared to primary aggregates, this morphology enhances packing efficiency and reduces uncontrolled scattering.
(2) Feeder geometry and vibration: The conical feeder, combined with precisely tuned vibration (30 Hz), ensures a continuous and uniform material discharge across the width of the splitter inlet. The vibration amplitude, governed by input voltage, further stabilizes the flow rate.
(3) Splitter configuration: The splitter is engineered with symmetrically arranged triangular slots, enabling balanced bifurcation of material streams. This symmetry ensures that the RCA is distributed evenly, forming two concurrent and structurally similar piles.
(4) Conveyor synchronization: The movement of the conveyor belt is synchronized with the material discharge rate, facilitating the formation of uniform piles. Improper synchronization could result in pile deformation or layering inconsistencies.
(5) Gravitational and frictional forces: The downward movement of particles under gravity, combined with inter-particle and surface friction, supports consistent deposition and contributes to pile shape stability.

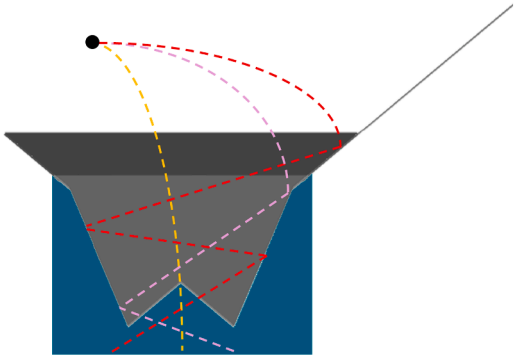

Fig. 3. Schematic cross-sectional diagram for RCA entering the splitter.

These combined factors ensure that the RCA is distributed in a physically predictable and geometrically stable manner, which is essential for maintaining the integrity of real-time PSD measurements.

In summary, the uniform distribution and stable formation of triangular RCA piles result from the combined effects of particle morphology, mechanical design of the feeder and splitter, vibrational dynamics, and physical interactions governed by motion and friction. As illustrated in Fig. 4(b), each half-layer—particularly the top layer—can be considered representative of the overall flow in terms of PSD and composition.

Although the feeding system, comprising the conical feeder and symmetric splitter, is engineered to minimize particle clustering and promote uniform material distribution across the conveyor width, it cannot fully eliminate localized variability. The system is designed to achieve a symmetrical layout within each half-layer of the pile while maintaining a consistent slope angle. However, experimental observations revealed a PSD gradient within the pile: finer particles tend to accumulate toward the central region, whereas coarser particles are more frequently deposited near the sides. This spatial segregation arises from size-dependent trajectory behavior during the feeding process. Smaller particles, due to their lower inertia and higher response to vibrational energy, are more likely to follow direct vertical paths and settle centrally. In contrast, larger particles experience greater deflection from splitter surfaces and are redistributed toward the edges.

This size-based segregation mechanism, consistent with established principles of granular flow under vibrational influence, contributes to the internal heterogeneity observed within the pile. While the system effectively reduces global nonuniformities, localized deviations in PSD remain, particularly along the pile slope.

3.2.2. 3D scanning system

To capture the 3D surface profiles of RCA piles during transportation, a Gocator 3D laser line scanner was mounted above the conveyor belt, as illustrated in Fig. 5. The sensor was positioned at a quarter of the conveyor width from the belt edge, providing optimal coverage of one side of each RCA pile for surface reconstruction and subsequent PSD estimation.

The resolution of the resulting point cloud data varies across three axes: along the belt (lengthwise), across the belt (widthwise), and in height (depth). The longitudinal resolution—along the direction of belt movement—is influenced by two factors: the belt speed and the encoder resolution of the Gocator system. The belt was driven by a motor operating at 50 Hz with a 4-pole configuration, yielding a motor speed of 1500 rpm. With a gearbox ratio of 19 and a drive wheel perimeter of 402.116 mm, the resulting belt speed was calculated to be 0.529 m/s.

The encoder resolution was configured at 1024 ticks per revolution. Under this configuration, the longitudinal point cloud resolution was determined to be 0.393 mm.

The lateral resolution across the width of the conveyor belt depends on the sensor's field of view and working distance. In this study, the resolution ranged between 0.375 mm and 1.100 mm, with a selected effective value of 0.378 mm. For the vertical (height) axis, the Gocator was set to maintain a fixed resolution of 0.083 mm.

These scanning parameters ensured sufficiently high spatial resolution for accurate 3D surface modeling of RCA piles under dynamic,

(a) Cross-sectional view *(b) Layered formation*

Fig. 4. RCA piles.

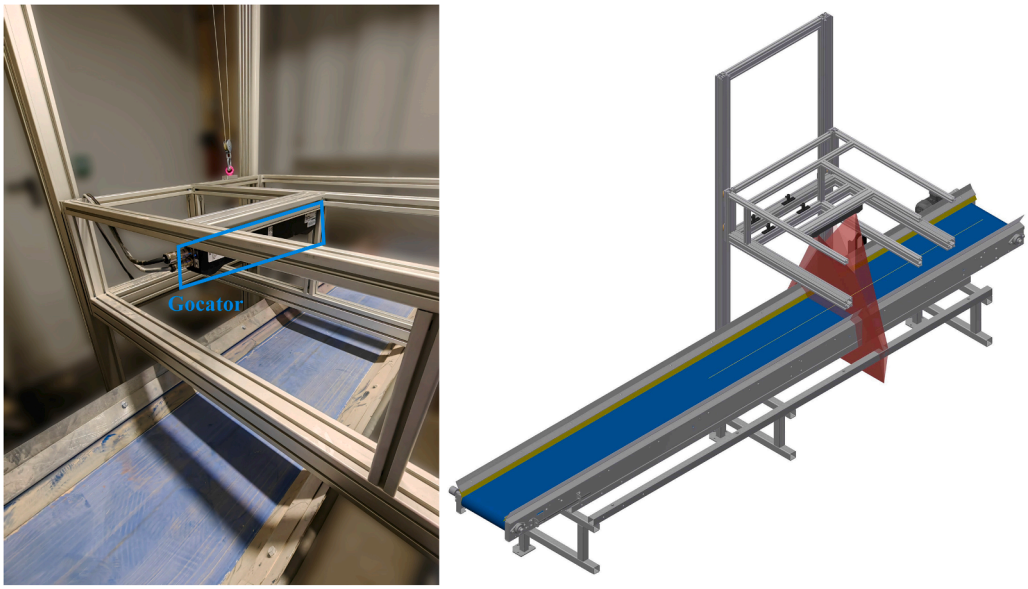

(a) Close view *(b) 3D view*

Fig. 5. 3D scanning system.

industrial-scale conditions.

3.3. Representative sampling methods

To enhance the efficiency and accuracy of PSD measurement via 3D surface scanning, a method was developed to estimate the PSD of an entire RCA pile based on analysis of a localized surface region. This required identifying sampling areas that provide statistically representative particle distributions.

Understanding the formation behavior of the piles is critical. The conical outlet of the silo (Fig. 2(a)) induces a radially outward flow of RCA, such that each particle type has an equal probability of being distributed across the perimeter of the vibrating feeder. Following passage through the splitter, particles are deposited in layers that form symmetric triangular piles. Since these piles are formed at a stable angle of repose, the uppermost layer—particularly its side surface—is likely to contain a representative cross-section of particle centers of mass. However, due to segregation effects, particle size and composition still vary from top to bottom within the pile.

Moreover, although surface-visible particles from the pile's side may appear representative, their actual contribution to the volume distribution must be verified. Therefore, a systematic approach was applied to determine whether a specific surface zone can serve as a reliable proxy for estimating the full PSD of the RCA pile. The procedure included the following steps:

(1) Comparative PSD evaluation: The PSD of the full side surface was analyzed and compared with the PSD of the entire pile to determine the degree of representativeness.
(2) Visual particle identification: The target surface region was marked using white spray paint (Fig. 6). Only particles with >70 % of their surface visibly covered from one side were selected for manual sieving, enabling clear isolation of the sampling region.
(3) Sampling strip selection: Narrow surface strips (20 mm wide) were extracted from multiple vertical positions on the pile, including the top, one-third, middle, and two-thirds heights. The bottom layer, where small particles were overrepresented and randomly scattered, was excluded due to its non-representative nature.
(4) Reference sieving analysis: Manual sieving using standard circular sieves was performed on both the selected surface strips and the entire pile. Particles were categorized into predefined size classes, and mass retention was recorded per fraction.
(5) Identification of representative zone: By comparing the PSD curves of all sampled regions with that of the full pile, the zone offering the closest statistical match was identified as the most representative sampling location.
(6) Correlation model establishment: A numerical correlation was developed between the PSD of the representative surface region and that of the entire pile. This model enabled reliable estimation of overall PSD based solely on surface analysis, significantly reducing data acquisition and processing requirements in practical applications.

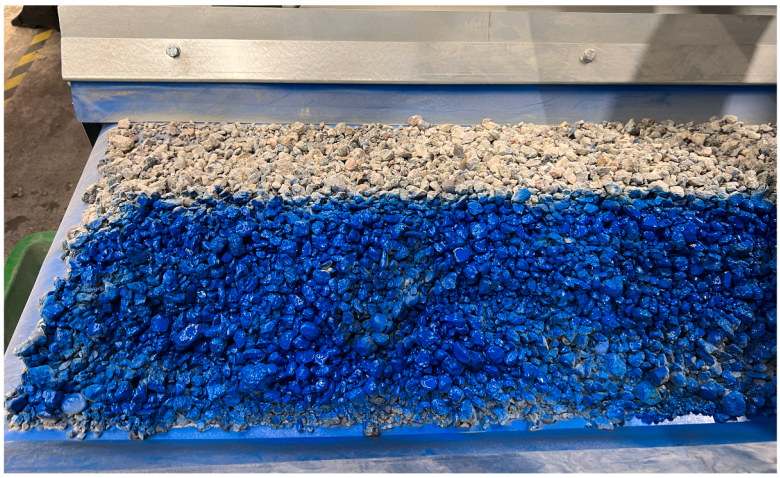

(a) Painting on the full side surface

(b) Painting on one-third and two-thirds distance from the top

(c) Painting on the top of the side

Fig. 6. Sampling from the side surface of the RCA piles.

3.4. Analysis methods

3.4.1. Particle segmentation and feature extraction

To obtain detailed morphological data from the selected sampling region, the 3D scanner (Gocator) was employed to generate high-resolution point cloud data of the RCA surface. To assess the validity of surface-based PSD estimation, comparative experiments were performed between full-depth manual sampling and surface-only measurements. As previously described, the RCA piles were formed under controlled flow conditions using a conical feeder and splitter, resulting in symmetric triangular piles deposited at a constant rate. This configuration significantly reduced observable segregation within the analyzed region.

Paint-based visibility tests confirmed that a strip located one-third from the top of the pile exhibited strong alignment with the overall PSD of the pile. Based on these findings, a correction procedure was introduced to compensate for residual underrepresentation of fine fractions in the surface layer. This adjustment ensures that surface-derived PSD estimates closely approximate the true bulk distribution, thereby validating the feasibility of non-invasive, strip-based PSD analysis for industrial applications.

This research adopts and improves the single flow algorithm [72,73] by adapting it to the actual morphological characteristics of RCA particles. The single flow algorithm is a commonly used method in terrain analysis for hydrological modeling. The enhancements made in this study enable a rapid and efficient 3D surface analysis of the 3D point cloud data. This method assumes the path of the steepest slope for point direction and records these directional paths as topologically ordered vectors of indices. The objective is to extract the size information of each particle by applying a parallel watershed segmentation [74,75] to the obtained 3D point clouds. This segmentation process separates the 3D point clouds into distinct regions, each representing an individual particle, or, if the particle is not strictly convex, a part of a particle. Over-segmentation is corrected based on proximity, neighbor relations, and surface orientation similarity. The regions corresponding to a single particle are then modeled with ellipsoids to create a representation of the particle that is suitable for estimating its shape factor, screen size, and volume. Fitting ellipsoids allow for a quantitative description of particle morphology. The length of the second shortest axis of the fitted ellipsoid is adopted as the gradation parameter for the particles. This parameter provides a measure of particle size, which is crucial for constructing the PSD. The process, illustrated in Fig. 7, involves several key steps.

Several key factors influence the accuracy and reliability of PSD results obtained from 3D point cloud data processing. First, the resolution and accuracy of the 3D scanner significantly impact the detail and

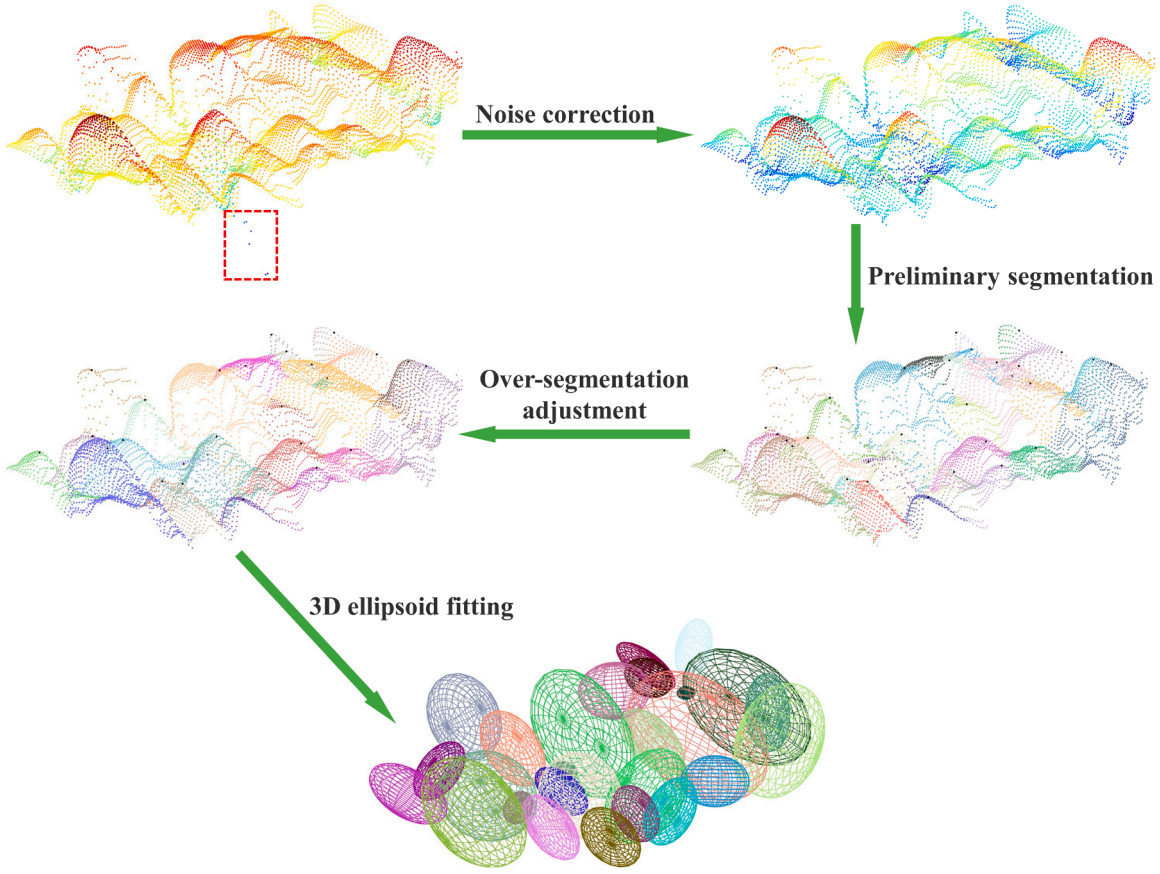

Fig. 7. 3D point cloud data processing.

precision of the point cloud. Higher resolutions in the conveyor belt direction, horizontal (across-belt), and vertical axes yield more precise particle segmentation results but may increase data volume and computational load. Second, the quality of raw point cloud data, particularly concerning noise and outliers, is critical. Noise arising from scanner reflectivity variations or gaps between particles can cause segmentation inaccuracies, which must be addressed by applying noise filtering and data smoothing techniques. Third, the choice and performance of the watershed segmentation algorithm directly determine the segmentation accuracy. The algorithm's sensitivity to parameter settings, such as minimum detectable particle size and the steepest ascent criteria, can lead to over-segmentation or under-segmentation issues. Thus, careful optimization of these parameters is essential. Fourth, the effectiveness of the criteria used for merging over-segmented particle regions significantly influences the correctness of PSD estimation. The merging approach relies on proximity thresholds and curvature continuity, necessitating precise calibration to prevent incorrect merging or exclusion of true particle segments. Lastly, the adopted ellipsoid fitting methodology affects the final particle size estimation, as the selection of ellipsoid axes for defining particle dimensions and the treatment of outlier fits with unrealistic dimensions strongly influence PSD accuracy. By systematically addressing and optimizing these five factors, the proposed method achieves reliable PSD characterization of RCA, providing critical support for effective quality assurance in concrete recycling operations.

The watershed segmentation method distinguishes itself from the local maxima-based method, which relies only on identifying the highest neighboring points, by incorporating gradient information and global topological data. This combination leads to more accurate and robust segmentation results. Although both methods initiate from local extrema, the watershed segmentation method shows better performance, particularly in areas with complex topologies. The key distinctions between the two methods can be explained through the following aspects:

(1) Segmentation foundation: The watershed segmentation method adopts a global approach by considering not only local extrema but also the overall gradient and flow direction of the particles. It simulates water rising from local minima, effectively "flooding" the entire region. This approach takes into account the entire topological structure of particles from the beginning, ensuring that segmentation is influenced by the overall shape and characteristics of the particles, rather than just local features. This allows it to form regions that are topologically coherent and consistent with the overall shape of the particles. The local maxima-based method identifies local peaks in the dataset and uses these peaks as the starting point for segmentation. However, when applied to complex topologies, it often misses important details, especially when dealing with irregularly shaped particles. The reliance on only local features limits its ability to accurately segment more intricate datasets.
(2) Boundary formation: Since the watershed segmentation method is driven by water flow paths based on gradient information, the segmentation boundaries form naturally at points where the flow from different basins converges (i.e., along the watershed lines). This boundary formation mechanism ensures that the segmentation respects the overall structure of the particles, resulting in smooth and natural boundaries. In contrast, local maxima methods may produce irregular or jagged boundaries, particularly when dealing with complex regions.

By integrating global topological information and gradient-based

flow, the watershed segmentation method provides a more robust and accurate segmentation process, especially in complex environments where the local maxima-based method might struggle to deliver precise results.

The 3D point cloud processing methodology adopted in this research extends previous watershed segmentation techniques by specifically addressing the practical challenges of RCA characterization under continuous industrial conditions. Previous studies typically applied segmentation algorithms to static or simplified particle configurations, whereas the current study focuses explicitly on dynamic RCA particle piles transported via conveyor belts, which present unique complexities including particle overlap, irregular shapes, and heterogeneous surface geometries. To effectively handle these conditions, an optimized watershed segmentation approach is proposed, incorporating a customized over-segmentation adjustment based on detailed particle proximity and local curvature criteria. Furthermore, ellipsoid fitting is utilized for morphological characterization, adopting the second shortest axis length to align computationally derived PSD directly with traditional industry-standard sieving practices. This integration of advanced computational techniques with established industrial quality control methods contributes directly to real-time, robust, and precise RCA quality assessment and optimization.

3.4.1.1. Noise correction. In 3D point cloud data analysis, the precision and consistency of the data are critical. Noise and outliers often lead to measurement errors, which significantly affect the analysis results. For instance, when measuring gaps between particles, the Gocator might capture lower reflectivity, leading to unusual values (as shown within the red dashed box in Fig. 7). These errors not only impact the assessment of particle size and distribution but also interfere with the analysis of other geometric properties. To improve the reliability and consistency of the results, it is essential to apply preprocessing methods such as noise filtering and data smoothing. These methods help refine the data, making it both more accurate and consistent.

In particular, outliers in the dataset—typically arising from irregular reflections, gaps between aggregate particles, or transient inaccuracies from the 3D scanning device—can significantly distort particle size estimations by incorrectly segmenting particles or creating artificial particle boundaries. To robustly address this issue, we implemented a linear interpolation technique to systematically correct abnormal z-axis measurements, effectively smoothing sudden deviations caused by measurement anomalies. Furthermore, clear and scientifically derived thresholds were established to automatically detect and exclude extreme outlier data points during the subsequent ellipsoid-fitting process. By combining interpolation-based smoothing and threshold-based outlier exclusion, the refined methodology significantly mitigates the detrimental effects of outliers on the final particle segmentation and PSD calculations, thereby enhancing the precision and reliability of our analytical results.

It is important to note beforehand that handling these noise and outliers is crucial during the initial segmentation process, as it ensures a smoother workflow. However, in the later stage of over-segmentation adjustment, the actual values of the data become essential. They represent the physical gaps between two particles, helping to accurately differentiate between a concave hull, as shown in Fig. 10(b), and the case of two adjacent particles. This distinction reduces the likelihood of incorrect merging.

The base surface of the entire point cloud needs to be horizontally aligned beforehand. Since the slope angles of the generated RCA piles are relatively consistent, this characteristic can be leveraged to reorient the base surface of the point cloud easily. This process ensures that the base surface is perfectly horizontal, with its normal vector pointing vertically upwards.

In the context of 3D point cloud data collected by the Gocator, the x and y coordinates form a structured grid while the z-axis represents varying height or depth measurements. Typically, noise and outliers stem from abnormal z-axis values. Managing these erroneous z-values is critical for maintaining the integrity and utility of the data. To address this issue, linear interpolation is employed across the grid to estimate abnormal z-values based on their spatial arrangement and adjacent data points. This method is well-suited for the data's structured nature, characterized by regular spatial intervals.

The process of interpolating abnormal z-values accounts for both horizontal and vertical spatial relationships to preserve the integrity of the data's surface geometry. For each missing or negative z-value, interpolation is performed by forming a plane defined by at least three surrounding points that are not collinear. The interpolated z-value at any given point $P_i\ (x_i,\ y_i,\ z_i)$ on the grid is then calculated using the formula derived from the plane equation:

$$z = a_p + b_p x + c_p y \tag{1}$$

where a_p, b_p, and c_p are coefficients determined by the known z-values of the neighboring points. This strategy ensures that the interpolation considers the gradient changes both along the x and y axes, providing a smooth transition across the grid. To ensure completeness, any remaining points with abnormal values at the boundaries or within the dataset, which could not be interpolated due to lack of neighboring data points, are addressed by backward and forward filling methods.

This interpolation method guarantees that all data points are filled and positive, reflecting plausible physical measurements. The use of linear interpolation offers a straightforward and computationally efficient approach to handling missing or erroneous data points. It also preserves the geometrical and topological consistency of the dataset, which is imperative for subsequent analytical tasks such as surface reconstruction, volumetric analysis, and visualization.

3.4.1.2. Preliminary segmentation. The objective of preliminary segmentation is to rapidly divide the 3D point clouds into different areas by sequentially adding points to the local highest point. Each area includes a local highest point, facilitating the establishment of computational orders for the points that represent the shape of particles. The segmentation creates a structured dataset with particles represented by local high points and their associated downhill points. The preliminary segmentation process can be broken down into several key conceptual steps: (1) Identification of the local highest points: This step involves identifying the local highest points within the 3D point cloud. These local highest points act as the starting points for defining individual particle segments. (2) Calculation of the steepest ascent path: For each point in the 3D point cloud, the path of the steepest ascent towards the nearest local highest point is calculated. This determines the grouping of points into potential particle segments. (3) Segment formation: Based on the paths of the steepest ascent, points are grouped into segments that are associated with the local highest points identified earlier.

(1) Identification of the local highest points

Using the coordinates of each point P_i , the algorithm scans the surrounding points to identify the highest elevation within the defined k_p neighborhood. This local maximum TP_i is designated as the highest point for that region.

Each point on the surface of the particles is denoted by its coordinates $P_i\ (x_i,\ y_i,\ z_i)$. For every point P_i , there is a corresponding particle, denoted as a set of points $N(P_i)$, which contains the total number of n_p points. Among these, TP_i is identified as the local highest point. To Identify the local highest points, it is important to determine the uphill point for each point P_i .

Uphill point, UP_i: For each point P_i , the uphill point is the neighboring point where the point path direction goes to, identified by the steepest ascent from P_i . The steepest ascent to a neighboring point $P_j\left(x_j,\right.$

$y_j,\ z_j\big) \in N(P_i)$ is calculated using the gradient formula:

$$d_{ij} = \sqrt{(x_j - x_i)^2 + \left(y_j - y_i\right)^2 + (z_j - z_i)^2} \tag{2}$$

$$\Delta z_{ij} = \frac{z_j - z_i}{d_{ij}} \tag{3}$$

where d_{ij} is the Euclidean distance between points P_i and P_j. Each point P_i evaluates its neighboring points to determine its uphill point based on the steepest ascent:

$$UP_i = \arg \max_{p_j \in N(P_i)} \Delta z_{ij} \tag{4}$$

The point with the highest positive gradient value Δz_{ij} represents the steepest ascent from P_i .

By calculating the steepest ascent for each point P_i to its k_p nearest neighbors, particles are initially segmented based on the local highest point representing their summits. Given that a small amount of fine material (2.0–4.0 mm) will be present in the targeted RCA product, the minimum visible surface area for a single particle should be around 3.1 mm^2. The Gocator sensor has a resolution of 0.393 mm and 0.378 mm in the horizontal plane, respectively. To establish a clear lower size limit for the visible particle area during segmentation, and considering that not all measurement points will precisely align with the particle surface—resulting in a slightly smaller area than 3.1 mm^2—the minimum k_p value is set at 20. This value covers an area of 2.971 mm^2, preventing the misinterpretation of larger particles as multiple smaller ones.

(2) Calculation of the steepest ascent path

Once the local highest points are identified, the next step is to calculate the steepest ascent path for each point in the 3D point cloud. This path determines the direction in which each point will "climb" towards its nearest local highest point. In this step, the dataset is organized into a structured format that allows for efficient access and manipulation. The sorting operation arranges the particles based on their spatial properties, preparing them for the segmentation algorithm. Additionally, an array, denoted as D, will be created to store all the downhill point information.

To perform this operation, the process assumes that the path direction goes uphill, following the path of the steepest ascent. For each point P_i , it is necessary to identify its downhill point set.

Downhill point set $DP_{i,d}$: For each point P_i , the downhill point set includes all points where their steepest ascent path direction goes to the point P_i . Here, $d = 1, \cdots, ND_i$, where ND_i is the total number of points, whose steepest ascent pathways converge at point P_i . Essentially, $DP_{i,d}$ comprises all points that consider P_i as their uphill point, as illustrated in Eqs. (5) and (6):

$$UP_{DP_{i,d}} = P_i \tag{5}$$

$$DP_{i,d} = \{P_j \mid UP_j = P_i\} \tag{6}$$

For each point P_i , initialize ND_i values to zero. This count will later be incremented based on the point path directions determined by the topology. Using the uphill point UP_i information, which specifies where each point P_i 's next direction goes to, the downhill point counts ND_{UP_i} for UP_i are then updated. Specifically, for each point P_i , once its uphill point UP_i is determined, the count of downhill points for UP_i is increased by 1. Specifically, ND_{UP_i} is incremented as follows:

$$ND_{UP_i} = ND_{UP_i} + 1 \tag{7}$$

This procedure is demonstrated using a single example consisting of nine points, as depicted in Fig. 8 and Table 2. Black dots represent the points in the 3D point cloud. Black dotted lines show all potential connections between neighboring points. Blue solid lines indicate the connections made according to the steepest ascent hypothesis (as shown by the arrows) used to construct the topology. Point 9 is assumed to be the local highest point in the area.

Then, transform the list ND_i into an index array Ψ, which contains the location of where the list of downhill points to point P_i is stored. The index array Ψ is constructed to facilitate quick access to the starting point of each point P_i 's downhill point list within a global list array D. The single dimension array D is used to store all the downhill point information $DP_{i,d}$. The array Ψ is built in reverse order, starting from the last point and moving to the first. The specific steps are as follows:

Table 2
Calculation of relevant parameters in Fig. 8.

P_i	1	2	3	4	5	6	7	8	9
UP_i	5	6	6	5	9	9	8	9	9
$DP_{i,j}$	/	/	/	/	1	2	/	7	5
	/	/	/	/	4	3	/	/	6
	/	/	/	/	/	/	/	/	8
	/	/	/	/	/	/	/	/	9
ND_i	0	0	0	0	2	2	0	1	4
Ψ_i	1	1	1	1	1	3	5	5	6

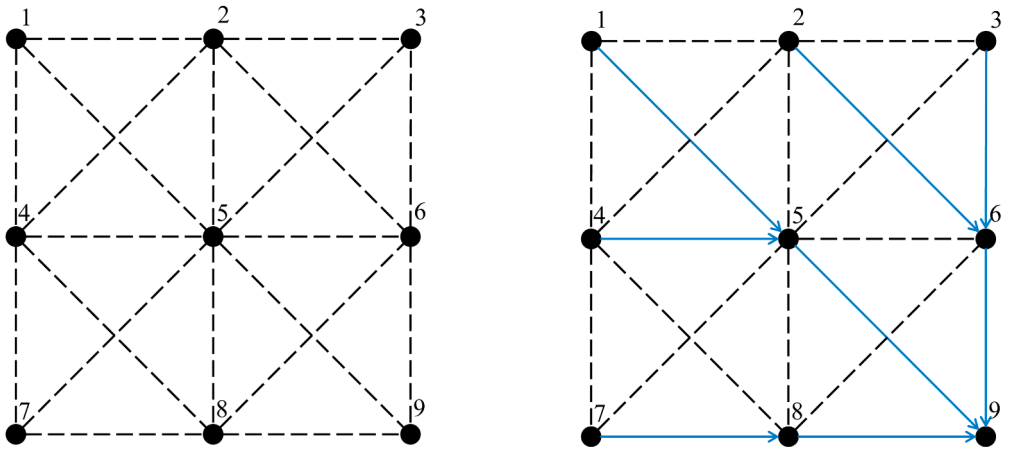

(a) Possible path directions (b) The steepest ascent path directions

Fig. 8. Top-down view of a 3D point cloud.

$$\Psi_{n_p} = n_p + 1 - ND_{n_p} \tag{8}$$

$$\Psi_{i-1} = \Psi_i - ND_{i-1} \text{ for } i = n_p, \cdots, 2 \tag{9}$$

This ensures that each point P_i 's downhill point set in D can be accessed using Ψ_i as the starting index. The initialization and updating of downhill point counts are operations that scale linearly with the number of points, making the algorithm efficient for large-scale models.

Store the count of how many times each point has been designated as the uphill point into an integer array Φ. Initialize this integer array Φ with all elements set to zero. For each point P_i , identify its corresponding uphill point UP_i. Once identifying UP_i, update D and Φ, and populate the downhill point list using:

$$D\left(\Psi_{UP_i} + \Phi_{UP_i}\right) = i \tag{10}$$

$$\Phi_{UP_i} = \Phi_{UP_i} + 1 \tag{11}$$

Here, Ψ_{UP_i} indicates the start of the downhill point in array D for the uphill point UP_i. This step effectively adds a point P_i to the list D of its uphill point UP_i and increments the count of downhill points for UP_i. Once all points have been processed, downhill point information of each point P_i can be retrieved using:

$$DP_{i,d} = D(\Psi_i + \alpha) \text{ for } \alpha = 0, \cdots, \Psi_{i+1} - 1 \tag{12}$$

Here, Ψ_i is the index in D where the downhill point list for point P_i starts, allowing sequential access to all downhill points of point P_i.

(3) Segmentation formation

In this step, points are grouped into segments based on the paths of the steepest ascent calculated in the previous step. Each segment corresponds to a particle, with points being grouped around their respective local highest points. The use of stacks and index arrays facilitates the efficient management of these groupings, allowing for rapid computation even with large datasets. The goal is to build a stack S that arranges points from the lowest point to the highest based on their dependencies in the point network. The stack helps to ensure that each point is processed in the correct order.

Initialize a stack S and set global variable index β initialized to 1. This index β will be used to track the current position in the stack S where points are added. For each top point TP_λ, $\lambda = 1, \cdots, n_\lambda$, initialize β to 1 and invoke the stack addition procedure for each downhill point of TP_λ using the list from the downhill point array D. Initiate the stacking process, this is done recursively:

$$add\_to\_stack(L_D, \beta) \text{ for } L_D = D\left(\Psi_{TP_\lambda}, \Psi_{TP_\lambda} + 1, \cdots, \Psi_{TP_{\lambda+1}} - 1\right) \tag{13}$$

where λ starts from each top point, and β is incremented within the *add_to_stack* function, which recursively adds points to the stack. The *add_to_stack* function is recursive, ensuring all points contributing to a top point are included before moving to points contributing to its downhill points, thus effectively creating a well-ordered process for boundary calculations.

Define and use the function $add\_to\_stack(L_D, \beta)$ to recursively add points to the stack:

$$S(\beta) = L_D \tag{14}$$

Continue adding downhill points of L_D recursively:

$$add\_to\_stack(\gamma, \beta) \text{ for } \gamma = D(\Psi_{L_D}, \Psi_{L_D} + 1, \cdots, \Psi_{L_{D+1}} - 1) \tag{15}$$

This recursion continues until a point is reached that has no downhill points.

This process builds the stack by ensuring that all points are added following their steepest ascent path directions, maintaining a natural order from downstream to upstream contributors. This process is recursive, meaning that whenever a point is added to the stack, all its downhill points are also added to the stack until no more downhill points can be added. Points without downhill points do not initiate further recursive calls, preventing unnecessary stack operations and ensuring the recursion remains bounded.

The stack stores the sequence of all points from 1 to n_p. Points are added to the stack in a specific order that reflects the physical shape of the particles. Importantly, the structure of the stack ensures that each point is visited exactly once, and the length of the stack is equivalent to n_p. The stack-building process can be parallelized by distributing the local highest points among multiple processors. Each processor constructs a segment of the stack independently.

The arrangement of the stack is displayed in Fig. 9(a) according to the scenario depicted in Fig. 8. From this example, it is evident that inverting the order of the points on the stack results in a reversed configuration (Fig. 9(b)).

By inverting the order of points in the stack, starting from points without downhill points (bottom points) and moving uphill, the computation can systematically handle each particle area. At each junction of the paths, if the junction includes uphill points, the inverted stack moves to the bottom of each lower branch. This allows for a systematic and step-by-step calculation of points from the lower areas before continuing past the junction. If there are no uphill points at the junction, the inverted stack moves to the bottom of another particle. This approach ensures that each point and its downhill points are calculated before moving upstream, enhancing the accuracy of the model. Eq. (16) represents the stack where points are stored in a specific order to be processed from the bottom points upward through the network.

$$S(i) \text{ for } i = n_p, \cdots, 1 \tag{16}$$

The n_p points are processed in an order that is appropriate to classify each point to the particle area. The inverted stack begins at the bottom points and proceeds uphill, following the steepest ascent path. These operations are performed in parallel, ensuring efficiency even for large datasets. Once completed, a total of n_λ particles are segmented.

The preliminary segmentation uses the steepest ascent algorithm to rapidly and efficiently segment 3D point clouds. By calculating the uphill and downhill paths for each point, the structure enables the creation of particle areas in an organized, computationally efficient manner. The stack construction ensures that points are processed in a logical order from bottom to top, facilitating large-scale model processing.

3.4.1.3. Over-segmentation adjustment. Fig. 10 illustrates cross-sectional views of point clouds obtained by scanning particles in two different states using the Gocator. In the diagram, the vertical gray lines represent the structured spacing formed by the Gocator during the scan along the x-axis, while the red and blue dots depict points captured on the surface of the particles. In Fig. 10(a), the shape described is a convex hull, which is round and smooth. In contrast, Fig. 10(b) shows a concave hull, characterized by indentations or inward curves.

During the preliminary segmentation process, particles with convex hull shapes are easily identified as a single particle due to their smooth and unbroken outlines. However, particles with concave hull shapes present challenges; when attempting to extract the local highest points, these shapes are prone to being mistakenly divided into separate segments, as shown in Fig. 10(b) with red and blue sections, resulting in the erroneous division into two particles. This leads to over-segmentation. To address this issue, it is essential to merge adjacent segments that originally belonged to the same particle to ensure accurate recognition and analysis.

To address the common issue of over-segmentation resulting from the initial watershed segmentation, particles are merged based on proximity, neighbor relations, and surface orientation similarity. Two neighboring particles are merged if they share a border, and the

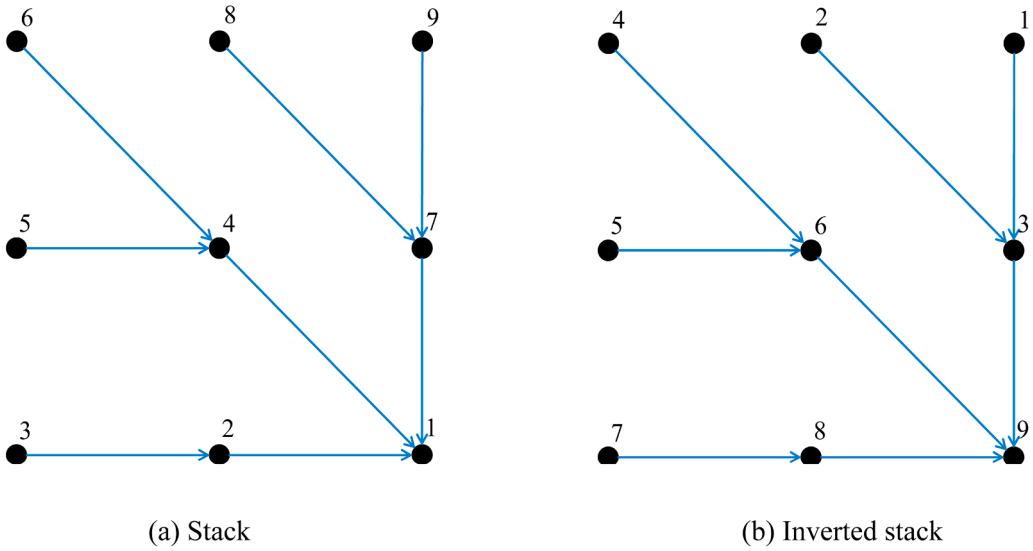

Fig. 9. Stack and inverted stack order.

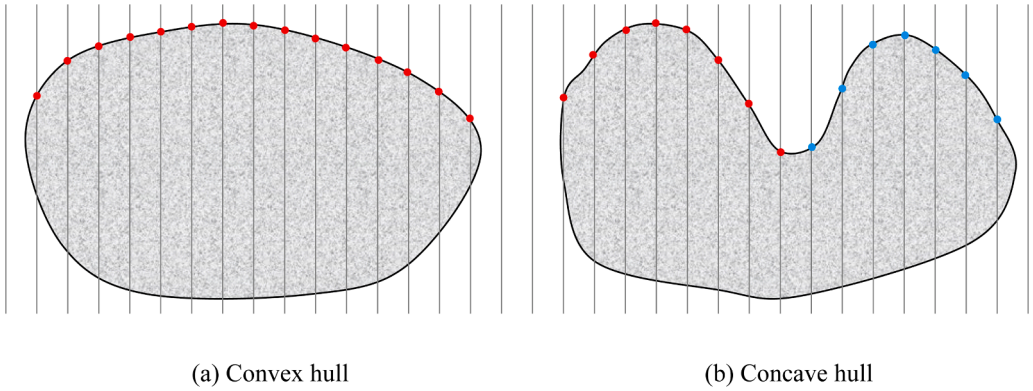

Fig. 10. Schematic cross-sectional diagram for 3D scanning of particles.

boundary points between them are continuous. This step ensures that particles over-segmented due to local topographic maxima or noise are accurately merged.

It is worth reiterating that, in this process, the previously smoothed values obtained using the interpolation method will no longer be used. Instead, the original values will be applied. This adjustment allows for more accurate identification of neighboring particles, preventing incorrect merging. Additionally, it helps to differentiate the concave hull scenario in Fig. 10(b).

After preliminary segmentation, two adjacent particles, designated as PA_u and PA_v ($u, v \in \{1, \cdots, n_\lambda\}$), to be merged into a single particle, they must meet the following proximity and continuity conditions: The distance between the boundary points of the two particles must be sufficiently small to ensure that the two particles share a border. Additionally, the average absolute difference in the local curvature at these boundary points should be below a certain threshold to maintain the continuity of the boundary.

When assessing the proximity and continuity between the boundary points of two adjacent particles PA_u and PA_v , merging is considered if the distance between the two particles' boundary points is <0.6 mm, which is derived from the Gocator's resolutions of 0.378 mm, 0.393 mm, and 0.083 mm. These values suggest that the maximum distance between two adjacent points in space is approximately 0.6 mm. Additionally, the boundary points of the two particles should have nearly identical local curvatures to ensure continuity.

Define BP_u as the set of boundary points in particle PA_u, similarly, define BP_v as the set of boundary points in PA_v. Let bP_{iu} be a subset of points in BP_u and bP_{iv} be a subset of points in BP_v that satisfy the following conditions: For each boundary point $bP_{iu} \in BP_u$, there exists a boundary point $bP_{iv} \in BP_v$ such that $\| bP_{iu} - bP_{iv} \| \leq 0.6mm$; Each bP_{iu} uniquely corresponds to the nearest boundary point bP_{iv}. This implies that bP_{iu} and bP_{iv} should appear in pairs. Define n_{iu} as the number of boundary points bP_{iu} in BP_u that meet these conditions, and n_{iv} as the number of boundary points bP_{iv} in BP_v that meet these conditions. Thus, we have:

$$n_b = n_{iu} = n_{iv} \tag{17}$$

Where n_b is the number of boundary points satisfying the conditions.

To calculate the local curvature at the point bP_{iu}, it's necessary to approximate the local surface using points in its vicinity. This involves using a spatial data structure, such as a KD-tree, to efficiently locate the k_b nearest neighbors of each point bP_{iu}. For this calculation, each point's neighborhood $N(bP_{iu})$ comprises the $k_b = 9$ nearest neighbors.

To model the local surface around each point bP_{iu}, an optimal quadratic polynomial is fitted using the least squares method, which is a technique that minimizes the sum of the squared differences between the observed values and the values predicted by the model. The general form of the polynomial is:

$$z = a_b x^2 + b_b y^2 + c_b xy + d_b x + e_b y + f_b \tag{18}$$

The coefficients a_b, b_b, c_b, d_b, e_b, f_b are determined to minimize the

squared error sum:

$$\sum_{ju=1}^{k_b}\left[z_{ju}-\left(a_b x_{ju}^2+b_b y_{ju}^2+c_b x_{ju}y_{ju}+d_b x_{ju}+e_b y_{ju}+f_b\right)\right]^2\rightarrow\min \tag{19}$$

where $\left(x_{ju},\ y_{ju},\ z_{ju}\right)$ are the coordinates of the points in the neighborhood $N(bP_{iu})$.

Once the surface is fitted, the first and second derivatives at each point are calculated to determine the local curvature. These derivatives are given by:

$$f_x=2a_b x+c_b y+d_b \tag{20}$$

$$f_y=2b_b x+c_b x+e_b \tag{21}$$

$$f_{xx}=2a_b \tag{22}$$

$$f_{yy}=2b_b \tag{23}$$

$$f_{xy}=c_b \tag{24}$$

The local curvature κ at each point can be estimated using the following formula:

$$\kappa=\frac{f_{xx}\left(1+f_y^2\right)-2f_{xy}f_x f_y+f_{yy}\left(1+f_x^2\right)}{2\left(1+f_x^2+f_y^2\right)^{\frac{3}{2}}} \tag{25}$$

Calculate the local curvature for all points bP_{iu} and bP_{iv} and compare these values. If the average absolute difference in local curvature is minimal, it is likely that the two particles are geometrically continuous and might belong to the same particle. The average absolute difference in local curvature $\Delta\kappa$ is defined as:

$$\Delta\kappa=\frac{1}{n_b}\sum_{iu,iv=1}^{n_b}\left|\kappa_{iu}-\kappa_{iv}\right| \tag{26}$$

If $\Delta\kappa$ is below a certain threshold (in this case, 3 mm^{-1}), the particles s are considered geometrically similar and may be candidates for merging. These procedures effectively assess and resolve merging challenges in the 3D point cloud data of the RCA surface.

It is important to note that this algorithm is not designed to offer a highly detailed and precise point cloud segmentation method. Instead, its primary purpose is to enable fast segmentation of the point cloud. In certain exceptional cases, such as the one shown in Fig. 11, the initial segmentation may mistakenly identify two separate parts as red and blue, even though they should be classified as a single particle. Points A and B indicate two vertices that have been incorrectly identified as separate parts. Clearly, these two parts do not satisfy the proximity and continuity conditions. As a result, they remain separated during the over-segmentation adjustment phase. We are currently unable to effectively merge these types of particles into a single entity based on the aforementioned criteria. Moreover, since RCA typically exhibit more irregular shapes compared to natural coarse aggregates due to residual cement mortar adhering to their surfaces, it is theoretically possible—though extremely rare—for two aggregates to become connected by cement residue, forming shapes similar to the one depicted in Fig. 11. Nevertheless, this specific scenario—in which two segments fail to merge effectively due to insufficient boundary proximity and continuity—would only realistically occur under particular and uncommon conditions, such as when these uniquely shaped particles are in a unique upright position with no other particles obstructing the view during the Gocator scanning. Given the infrequency and specific nature of these cases, their overall impact on the accuracy and reliability of the final PSD results is minimal, and it is therefore reasonable to disregard them in the context of this study.

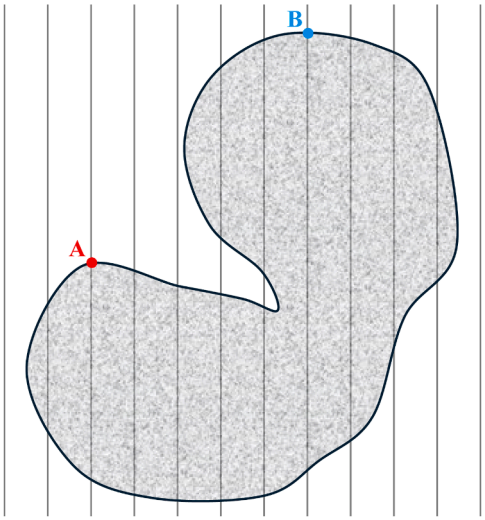

Fig. 11. Schematic cross-sectional diagram for the special case.

3.4.1.4. 3D ellipsoid fitting. Following segmentation, each particle's morphology is determined by fitting a 3D ellipsoid to describe the geometry of the particle. The optimal fit is achieved by minimizing the sum of squared distances from the points to the ellipsoid's surface, under constraints ensuring the surface represents an ellipsoid. The ellipsoid is defined by the equation:

$$a_e x^2+b_e y^2+c_e z^2+2f_e yz+2g_e xz+2h_e xy+2p_e x+2q_e y+2r_e z+d_e=0 \tag{27}$$

where x, y, and z are the coordinates of a point, and a_e, b_e,c_e, f_e, g_e, h_e, p_e, q_e, r_e, and d_e are the parameters that define the ellipsoid's shape, orientation, and position in the space. This fitting process involves a direct least-square fitting method and provides crucial morphological parameters such as the diameters of the major, intermediate, and short axes.

In ellipsoid fitting, flat or nearly flat surfaces tend to introduce greater uncertainty in the estimated parameters. To address this issue, if the calculated ellipsoid parameters, specifically the lengths of the three axes, significantly deviate from a reasonable range (with an upper limit of 22.4 mm), the result should be considered an outlier and filtered out. This process helps ensure that uncertainties in flat regions do not excessively impact the final ellipsoid parameters.

Finally, the cumulative percentage retained graph was plotted based on the volume of the fitted ellipsoid and the apparent density of the RCA. This graph depicted the PSD within the specific sampling area, which also represented the estimation of the overall PSD of the RCA piles.

3.4.2. PSD optimization

According to the European Standard [76], recycled aggregates used in concrete production must comply with specified upper and lower cumulative percentage limits across defined particle size intervals. As illustrated in Fig. 12, when the cumulative percentage retained curve of an RCA sample lies entirely within these specified bounds, PSD adjustment is not required.

However, in cases where the cumulative percentage retained curve of the RCA deviates from the allowable limits, a corrective adjustment is necessary to bring the PSD into compliance. Since the manual removal of specific particle sizes is labor-intensive and often impractical in industrial settings, the preferred corrective strategy involves the selective addition of supplementary material.

To optimize this adjustment process, a linear programming model is formulated. The objective of the model is to determine the minimal additional mass required in each particle size category such that the resulting cumulative percentage retained curve satisfies all standard-

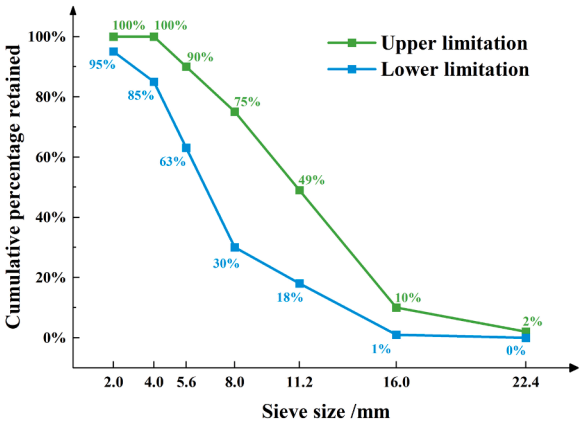

Fig. 12. Standard for cumulative percentage retained curves.

compliant bounds. This approach not only ensures regulatory conformity but also minimizes material consumption and operational effort.

The following section outlines the formulation and implementation of the linear programming-based PSD correction methodology.

(1) Variable definition

For a defined set of particle size intervals in ($in = 1, \cdots, 8$), we categorize the particle sizes into distinct intervals based on their diameter. Specifically: Interval 1 is defined for particle diameters greater than 22.4 mm. Interval 2 is defined for particle diameters from 16.0 mm to 22.4 mm. Interval 3 is defined for particle diameters from 11.2 mm to 16.0 mm. Interval 4 is defined for particle diameters from 8.0 mm to 11.2 mm. Interval 5 is defined for particle diameters from 5.6 mm to 8.0 mm. Interval 6 is defined for particle diameters from 4.0 mm to 5.6 mm. Interval 7 is defined for particle diameters from 2.0 mm to 4.0 mm. Interval 8 is defined for particle diameters <2.0 mm. Within each interval in, the variable w_{in} denotes the total weight of particles present within. A decision variable aw_{in} is defined to represent the weight of particles to be added to the particle size interval in.

(2) Objective function

The primary goal of the objective function is to minimize the total additional weight across all particle size intervals. The formulation of the optimal function is articulated as follows:

$$\text{Minimize} \sum_{in=1}^{tn} aw_{in} \tag{28}$$

subject to

$$W_{in} = \sum_{m=1}^{in} w_m + \sum_{m=1}^{in} aw_m \tag{29}$$

$$W_T = \sum_{jn=1}^{tn} w_{jn} + \sum_{jn=1}^{tn} aw_{jn} \tag{30}$$

$$CP_{in} = \frac{W_{in}}{W_T} \times 100 \text{ for } in = 1, \cdots, 7 \tag{31}$$

$$L_{in} \le CP_{in} \le U_{in} \tag{32}$$

$$aw_{in} \ge 0, \ \forall in \tag{33}$$

where tn is the total number of particle size intervals. Constraints (28) to (33) ensure that, for each particle size interval in, the current weight of particles w_{in}, in addition to the particles added through the variable aw_{in}, satisfies the cumulative percentage lower limit L_{in} and upper limit U_{in}.

Here, W_{in} signifies the total weight of particles across intervals 1 to in, while W_T represents the weight of all particles combined. CP_{in} denotes the cumulative percentage for interval in.

4. Results and discussion

This section presents and discusses the experimental results obtained from applying the proposed 3D surface analysis and PSD optimization method to RCA. The findings are organized to address key aspects of the methodology, including the representativeness of sampled surface areas, segmentation accuracy, estimation reliability, and performance of the linear programming optimization approach. The results are compared against manual sieving benchmarks to assess the system's effectiveness, and the implications for industrial application are also discussed.

4.1. Sampling data analysis

4.1.1. Representative sampling area identification

In the initial analysis, the PSD measured by manual sieving of the full side surface was compared and analyzed with the overall PSD of the RCA piles. Multiple experiments were performed on different batches of RCA to ensure reliable and representative results. The findings obtained from Fig. 13(a) demonstrated that there was no significant distinction between the two PSDs. Notably, the calculated root mean square errors (RMSE) for both tests were remarkably low, measuring only 2.05 % and 4.46 %, which indicated a high level of similarity. These outcomes strongly supported the conclusion that the PSD data acquired from measuring a single side of the triangular RCA piles could effectively represent the PSD of the entire RCA piles. Consequently, the observed consistency between the PSDs further consolidated the credibility and feasibility of inferring the PSD of the entire RCA piles based on the PSD measured at a specific area on the surface of the piles.

Analyzing the full side surface by point cloud analysis is computation-intensive, and therefore, it is attractive to consider a well-chosen strip of a limited width. After comparing and analyzing the PSD of different sampling areas on the side surface of various batches of RCA piles, it was observed from Fig. 13(b)-(e) that 20 mm wide strips taken at different positions—one-third distance from the top, two-thirds distance from the top, the top of the side, and the middle of the side—exhibited varying degrees of representativeness when compared to the overall PSD of the RCA piles.

It was evident that the PSD of the sampling areas tended to be overestimated when compared to the PSD of the entire pile. This discrepancy arose due to the behavior of the particles during the feeding process. Specifically, smaller particles have a tendency to roll down to the bottom of the pile, resulting in a higher concentration of particles in the 2.0–4.0 mm size range at the bottom section. As a result, there are relatively fewer 2.0–4.0 mm size particles in other regions of the pile's side surface. This uneven distribution of particles leads to a small percentage of mass in the 2.0–4.0 mm size range at most of the selected sampling areas. Consequently, when constructing the cumulative percentage retained curves, there is an overestimation of the PSD in this range.

Among these different sampling areas, the strips taken at the one-third distance from the top demonstrated the highest level of representativeness. The calculated RMSE for these strips was 4.10 % and 2.48 %, respectively. These values indicated a comparably minimal level of discrepancy between the PSD of the selected strips and the overall PSD of the RCA piles.

While the strips taken at the one-third distance from the top provided the most accurate representation of the overall PSD, it is important to note that there was still a certain degree of deviation between the curves of the selected strips and the overall PSD. This deviation, especially in the 2.0–5.6 mm particle size range, was particularly pronounced. Therefore, additional experiments were conducted to make necessary corrections and refine the accuracy of the obtained PSD data.

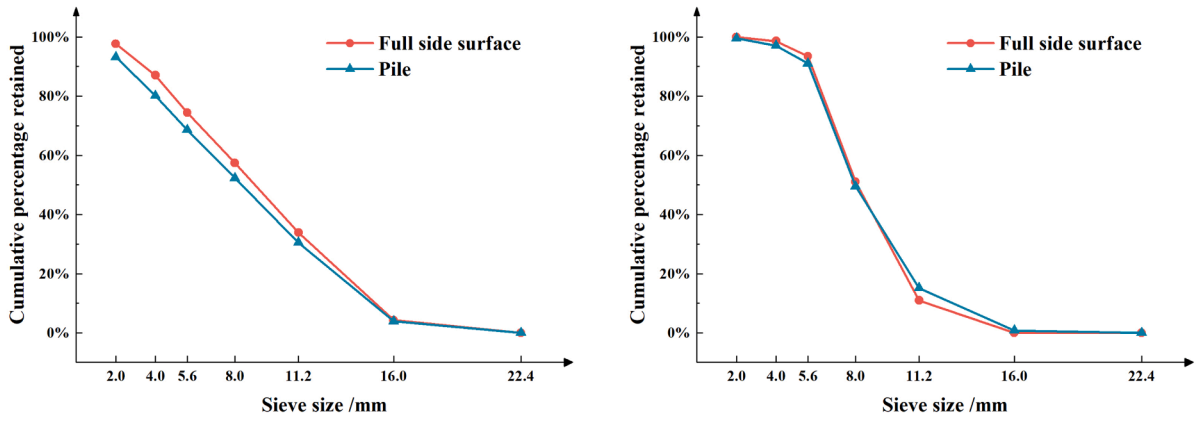

(a) Full side surface

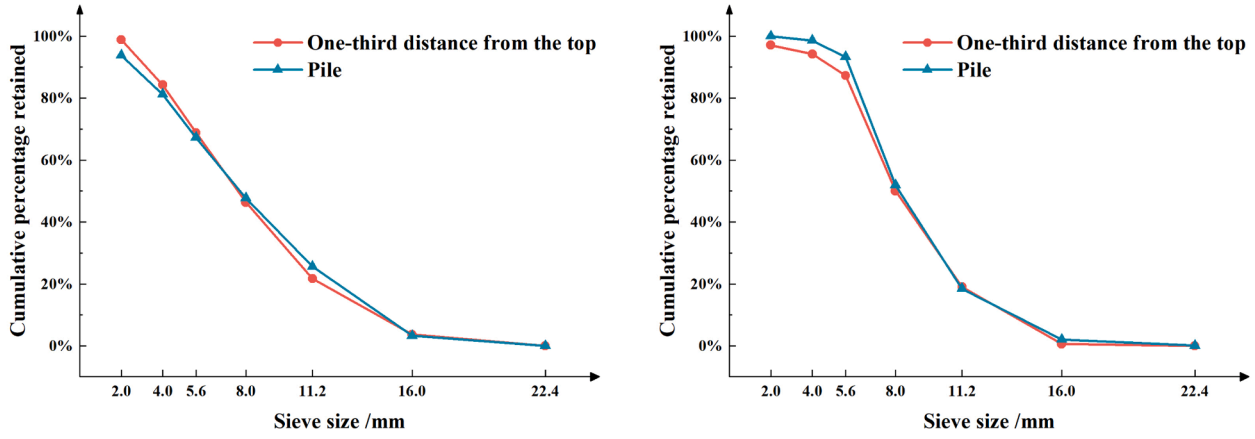

(b) One-third distance from the top

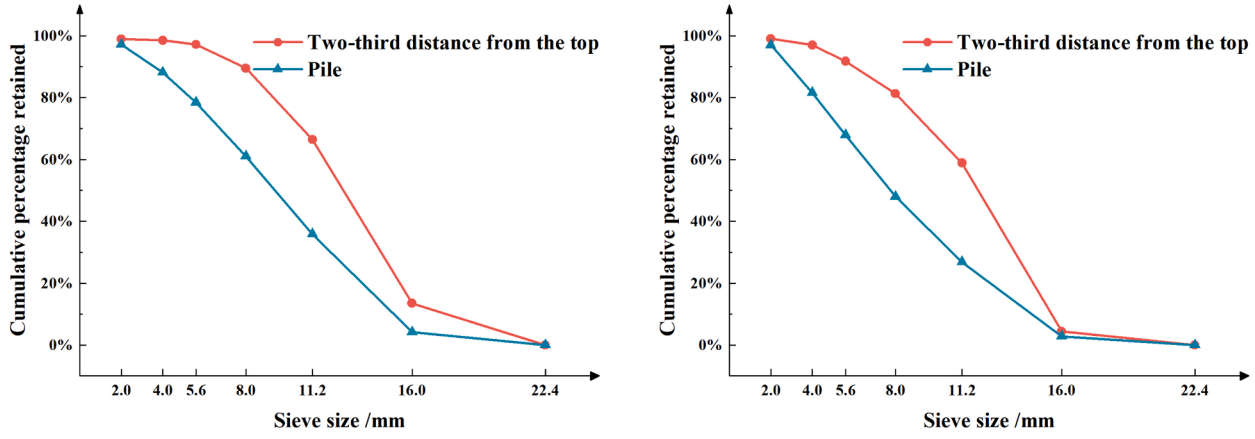

(c) Two-thirds distance from the top

Fig. 13. Cumulative percentage retained at different sampling areas.

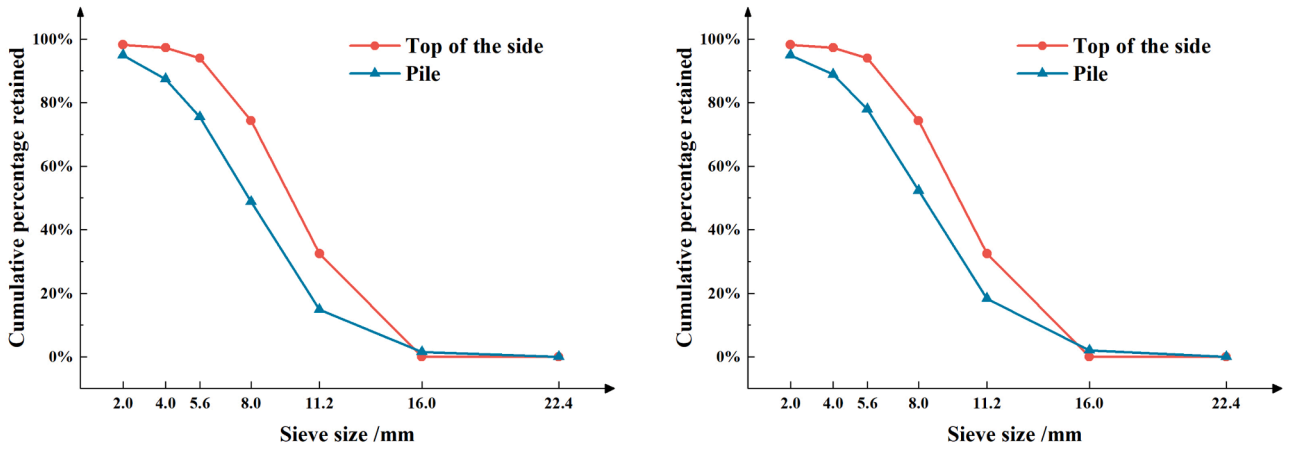

(d) Top of the side

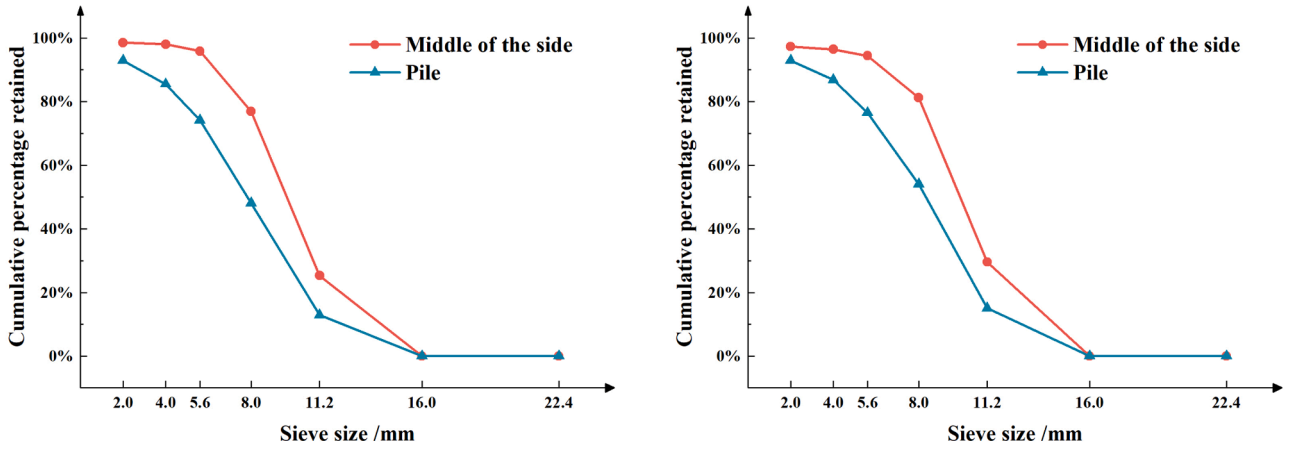

(e) Middle of the side

Fig. 13. (*continued*).

The observed results can be attributed to the utilization of the feeding system, which facilitates a uniform mixing and output of the RCA. As the RCA are transported onto the conveyor belt, it forms a triangular pile (Fig. 4(b)) that is generated layer by layer symmetrically and uniformly, starting from the inside and progressing toward the outside. This process allows for the deduction of the overall PSD by analyzing the PSD of a single full side surface of the outermost layer.

However, it is important to note that within each layer, there may be uneven separation, leading to variations in the PSD of different areas. Consequently, the PSD is not identical across different areas within each layer. More generally, when a different material is used or the same material is in different states (e.g., varying humidity levels), the PSD of the full side surface tends to be representative when employing this feeding method. In contrast, the areas of representative strips on the surface may not always be consistent, necessitating further experimentation for comprehensive analysis. In the present study, the RCA used were treated with the C2CA technique, ensuring a constant material state and allowing for consistent conclusions to be drawn.

4.1.2. Numerical relationship establishment

A total of sixteen sets of experiments were conducted using different batches of RCA, with samples taken at the one-third distance from the top of the RCA piles, marked and identified using paint to ensure consistent sampling. These samples, as well as the entire RCA piles, underwent manual sieving to obtain mass percentage data for different particle size ranges. The collected data of the sampled areas were then compared and matched with the corresponding data from the entire RCA piles, and the results were visualized in Fig. 14.

Additionally, a linear fitting was applied to establish a relationship between the sampled data and the overall data. Taking into account experimental errors and the impact of manual sieving, it can be observed that a certain linear relationship existed between the sampled data and the overall data within each particle size range. Leveraging the obtained linear relationship, each mass percentage data of sampled areas was corrected accordingly. However, due to the corrections made, the sum of percentages for each particle size range no longer added up to 100 %. Therefore, it was necessary to recalculate the percentage for each particle size range to ensure consistency. Table 3 provides a comparison of the results before and after the correction process. The comparison demonstrates a decrease in the RMSE for the curves representing the cumulative percentage retained of the sampled areas and the entire RCA piles. This reduction in RMSE values is particularly significant in cases

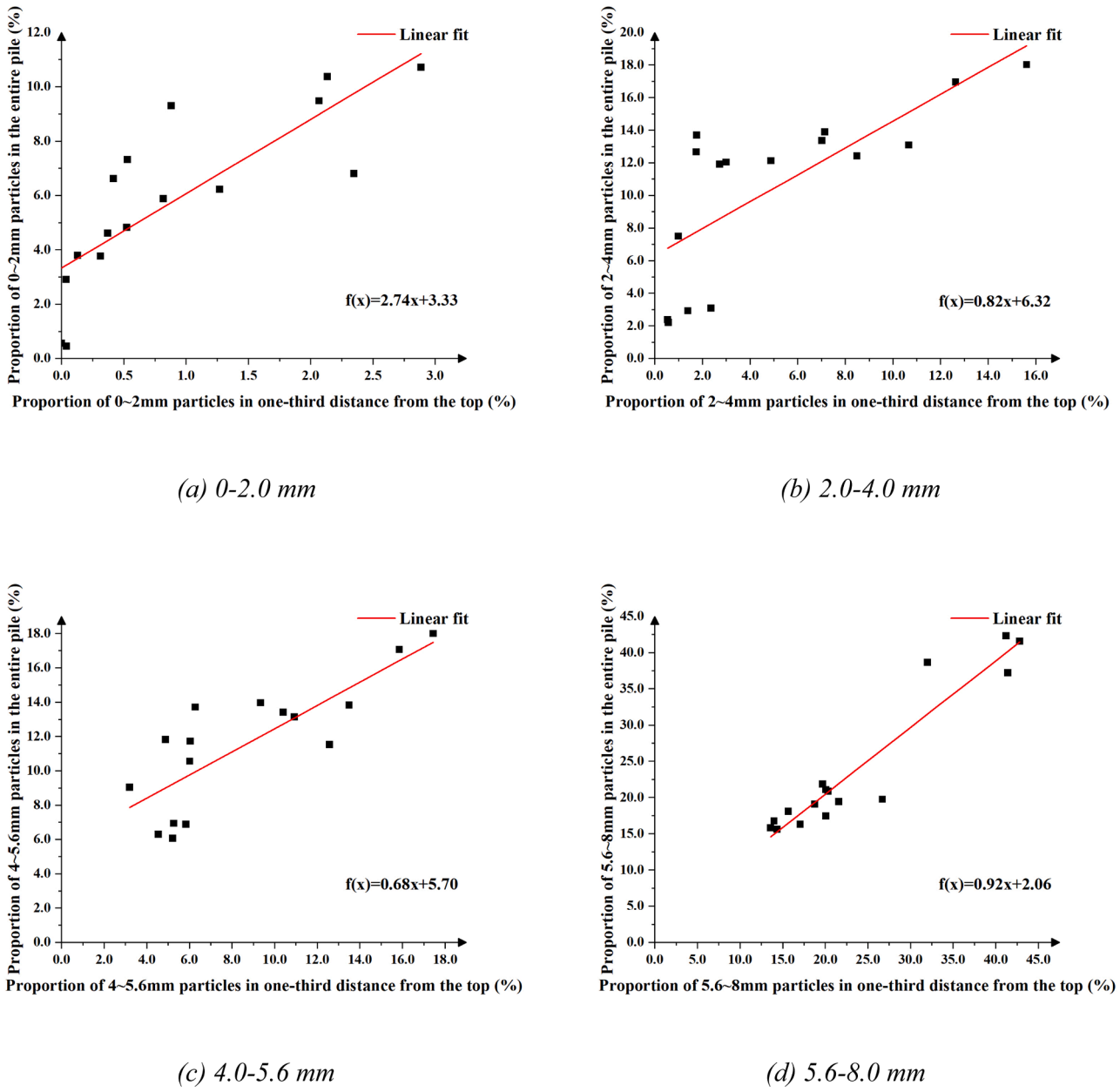

Fig. 14. The linear fit between the proportion of different-sized particles in one-third distance from the top and the entire pile.

where the initial RMSE was high, indicating a substantial improvement in the alignment between the curves. However, in cases where the initial RMSE was already low, the effect of the correction is relatively minor.

These findings highlight the importance of considering experimental errors and applying appropriate corrections to accurately represent the PSD of RCA piles. By refining the data through the analysis and correction process, the reliability and accuracy of the obtained results are enhanced.

4.2. PSD estimation

Fig. 15(a) presents the 3D point cloud data obtained from the 20 mm-wide strip located at the one-third distance from the top on the side surface of the RCA piles using the 3D scanner Gocator. To analyze the data, ellipsoids were fitted to the 3D point cloud data (Fig. 15(b)). The parameters of the fitted ellipsoids, specifically the lengths of three axes, were statistically analyzed. Among these parameters, the second shortest axis length was selected as the particle size parameter for particle counting. This selection was made to replicate the manual sieving process using circular sieves. By utilizing the second shortest axis length, the methodology aims to approximate the PSD in a manner consistent with traditional manual sieving techniques.

To obtain the cumulative percentage retained curves, it was necessary to determine the mass of each particle size range. The mass was estimated by calculating the volume and apparent density of each particle separately. The volume of each particle was estimated based on the volume of the fitted ellipsoids. Notably, during the estimation of particle mass, it was observed that smaller RCA particle sizes corresponded to higher apparent densities. To address this observation, a correction was applied to the mass of particles in different particle size ranges. By employing the correction method mentioned in the previous section, the mass percentages of each particle size range were adjusted accordingly. This adjustment facilitated the generation of the final cumulative percentage retained curves.

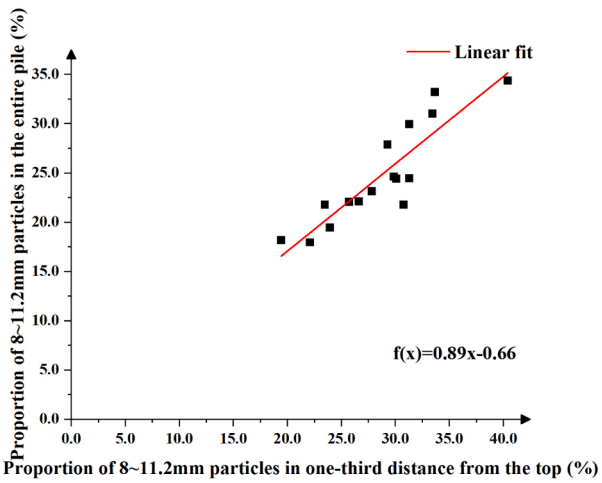

(e) 8.0-11.2 mm

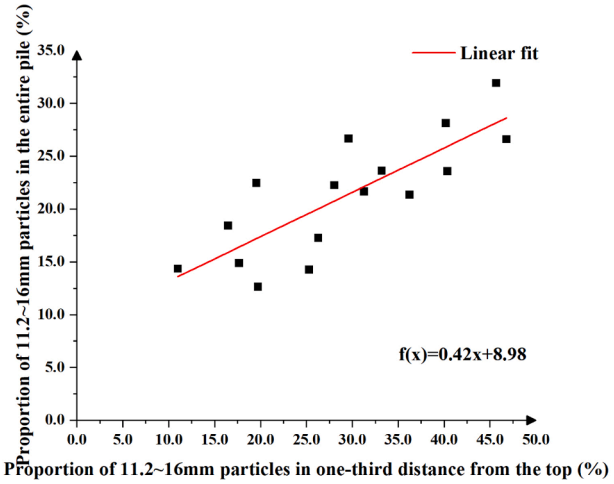

(f) 11.2-16.0 mm

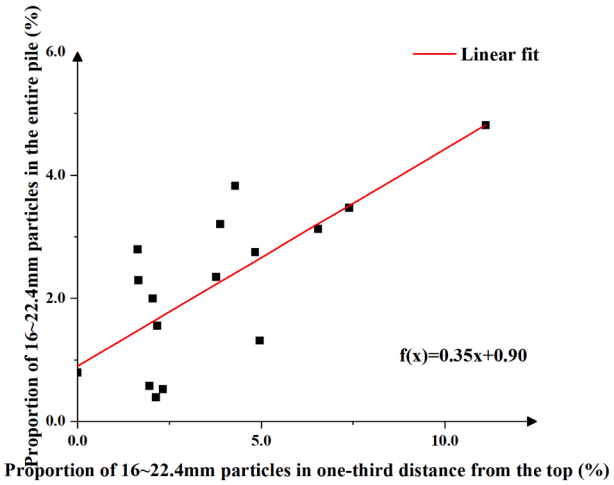

(g) 16.0-22.4 mm

Fig. 14. (*continued*).

Fig. 16 shows the comparison between the cumulative percentage retained curves predicted by the 3D point cloud data and those obtained by manual sieving, according to the results of three different pilot implementation scanning experiments. To evaluate the performance of the prediction method, the RMSE between the predicted values and the manually measured values were calculated for each experiment, yielding values of 5.26 %, 6.09 %, and 4.69 %, respectively. These RMSE values indicated the good performance and accuracy of the method in predicting the PSD of RCA piles on a conveyor belt.

Unlike static image-based techniques limited to single-layer or stationary particle analysis, this approach enables real-time, non-contact scanning and precise segmentation of overlapping particles within pile formations, even under high-throughput and high-speed industrial conditions. The reported RMSE values ranging from 4.69 % to 6.09 % are lower than the upper error margins of approximately 7 % documented in comparable studies [31,32,40], thereby affirming the reliability and effectiveness of the integrated watershed segmentation and ellipsoid-fitting framework.

4.3. Adjustment for optimal PSD

The above-mentioned predictions of the cumulative percentage retained curves are compared against the European Standard. From Fig. 17(a)(i), (b)(i), and (c), it is evident that among the three tests, the PSD in Test C meets the upper and lower limits of the EU standards, eliminating the need for additional adjustments. In contrast, Tests A and B fall short of these standards, necessitating the incorporation of RCA of varied particle sizes to achieve the required PSD, as delineated in Section 2.4.2.

Quantitative adjustments for Test A specify that for every 100.0 kg, an addition of 22.3 kg of aggregate is required in the 4.0 to 5.6 mm range, 18.9 kg in the 5.6 to 8.0 mm range, 18.9 kg in the 8.0 to 11.2 mm range, and 18.9 kg in the 11.2 to 16.0 mm range to meet the desired standards. Conversely, Test B necessitates a notably lesser augmentation, with only 0.7 kg of aggregate required in both the 2.0 to 4.0 mm and 4.0 to 5.6 mm ranges per 100 kg. Illustrated in Fig. 17(a)(ii) and (b)(ii), are the cumulative percentage retained curves post-aggregate

Table 3
The comparison of root mean square errors (RMSE) before and after the adjustment.

Root Mean Square Errors (wt %)	Before adjustment (wt %)	After adjustment (wt %)
Test 1	4.10	3.25
Test 2	4.57	3.97
Test 3	2.63	2.48
Test 4	4.41	1.63
Test 5	5.73	2.32
Test 6	5.68	2.13
Test 7	5.37	1.14
Test 8	5.50	1.43
Test 9	10.04	3.29
Test 10	3.46	1.63
Test 11	2.79	2.77
Test 12	6.54	0.54
Test 13	2.79	2.37
Test 14	7.01	1.45
Test 15	8.30	2.37
Test 16	8.14	5.48

addition, which successfully achieved optimal PSD.

We also compared the PSD results from RCA obtained from three distinct demolition sources. It was observed that RCA sourced from older infrastructures exhibited a higher proportion of smaller particles (2.0 to 8.0 mm), likely due to the advanced deterioration and increased brittleness of the parent concrete. In contrast, RCA derived from relatively newer structures displayed coarser and more uniform distributions. These source-specific variations underline the importance of carefully considering RCA origin characteristics during PSD evaluation and optimization. Incorporating source analysis into the PSD optimization strategy could further enhance the reliability and effectiveness of RCA use in concrete recycling operations.

4.4. Managerial insights

The implementation of a real-time 3D surface analysis and PSD optimization system for RCA processing offers substantial practical benefits, aligning with the principles of industrial information integration. This section delineates the key managerial insights derived from our study:

(1) Real-time quality monitoring and control: The integration of advanced sensing technologies enables continuous monitoring of RCA quality, facilitating immediate detection of deviations from desired specifications. This real-time feedback loop allows for prompt corrective actions, minimizing the production of substandard materials and reducing waste.

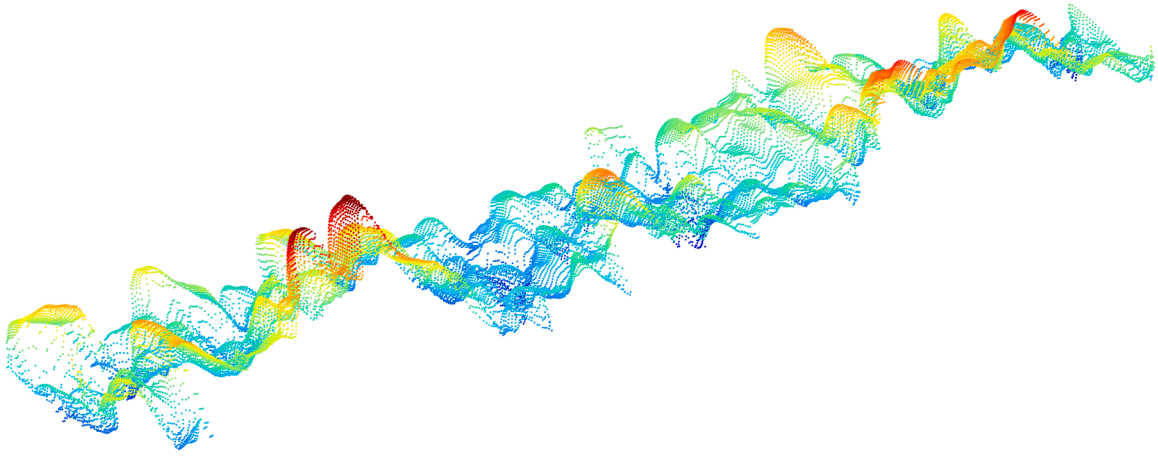

(a) 3D view of the 3D point cloud data

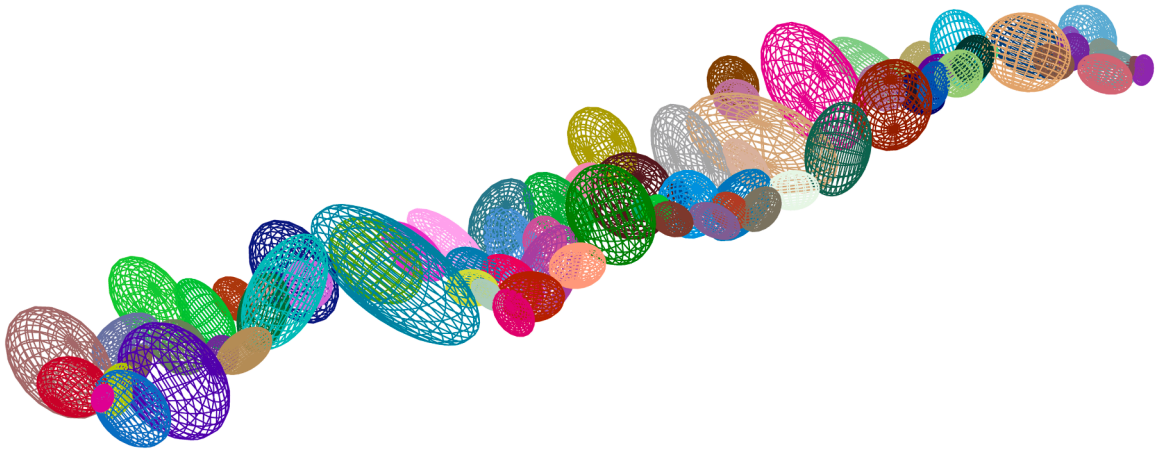

(b) Ellipsoids fitted to each particle

Fig. 15. 3D point cloud data processing.

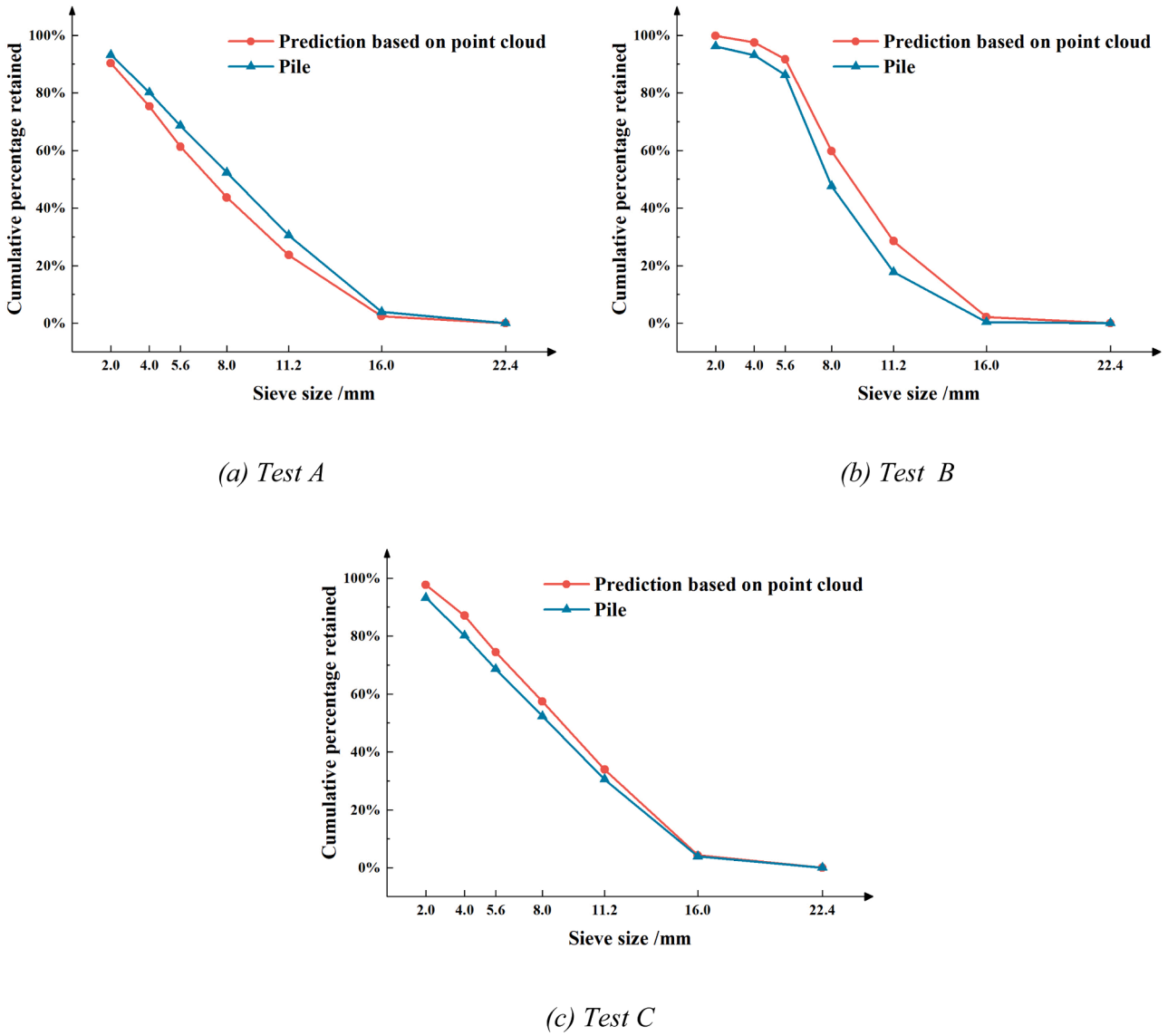

Fig. 16. Cumulative percentage retained curves.

(2) Enhanced decision-making through data integration: By consolidating data from various stages of the RCA processing pipeline, managers gain a holistic view of operations. This comprehensive data integration supports informed decision-making, optimizing resource allocation and improving overall process efficiency.
(3) Automation and labor efficiency: The automation of PSD analysis reduces reliance on manual sampling and laboratory testing, decreasing labor costs and mitigating human error. This shift towards automated quality control aligns with the broader industry trend of adopting smart manufacturing practices.
(4) Scalability and adaptability: The modular design of the system ensures scalability, allowing for seamless integration into existing infrastructure and adaptability to varying processing capacities. This flexibility is crucial for organizations aiming to expand or modify their operations in response to market demands.
(5) Sustainability and regulatory compliance: By optimizing the use of recycled materials and ensuring consistent product quality, the system contributes to environmental sustainability goals and aids in meeting regulatory standards. This alignment with sustainable practices enhances corporate social responsibility profiles and can provide a competitive advantage in environmentally conscious markets.
(6) Integration with enterprise systems: The system's compatibility with existing enterprise resource planning and manufacturing execution systems facilitates seamless data flow across organizational levels. This integration supports the synchronization of production schedules, inventory management, and quality assurance processes, embodying the core objectives of industrial information integration.

In summary, the deployment of this real-time 3D surface analysis and PSD optimization system not only enhances operational efficiency and product quality in RCA processing but also exemplifies the practical application of Industrial Information Integration principles. By fostering real-time data utilization, automation, and system interoperability, the approach contributes to the advancement of intelligent manufacturing and sustainable industrial practices.

5. Conclusion

This study introduces a fully integrated, industrial-scale solution for the intelligent optimization of PSD in unscreened RCA. Unlike most previous research, which focuses on static analysis or manually collected samples, our system enables real-time, non-contact 3D scanning of RCA

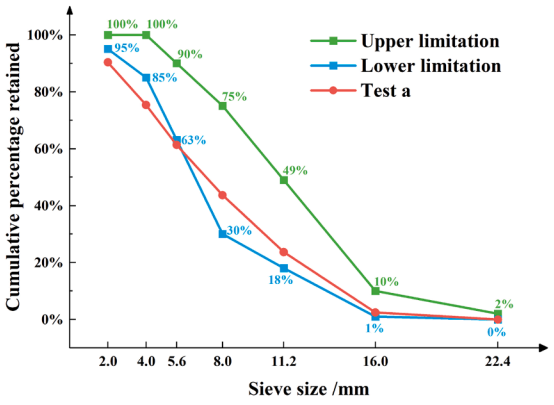

(i) Predicted by 3D point cloud data

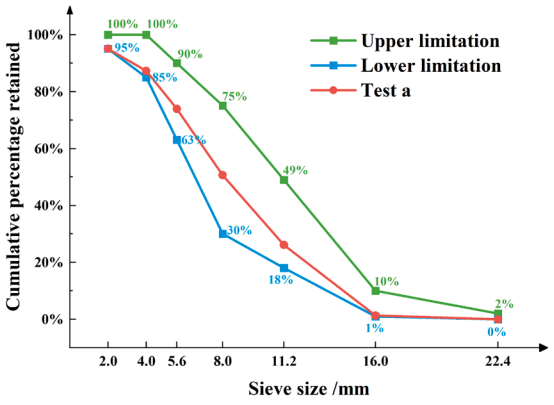

(ii) Adjusted for optimal PSD

(a) Test A

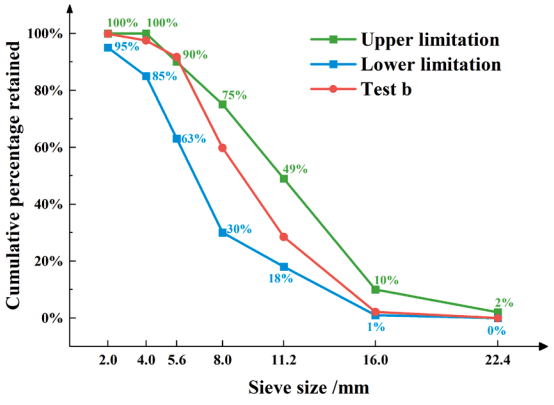

(i) Predicted by 3D point cloud data

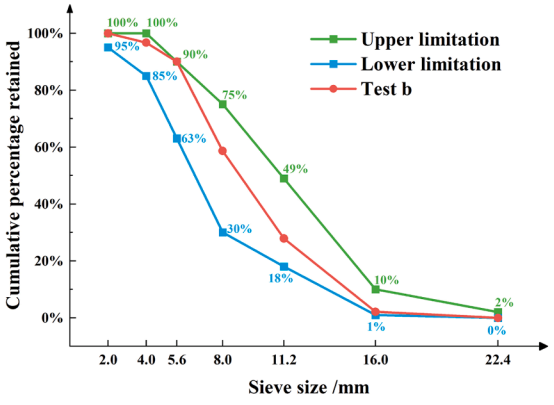

(ii) Adjusted for optimal PSD

(b) Test B

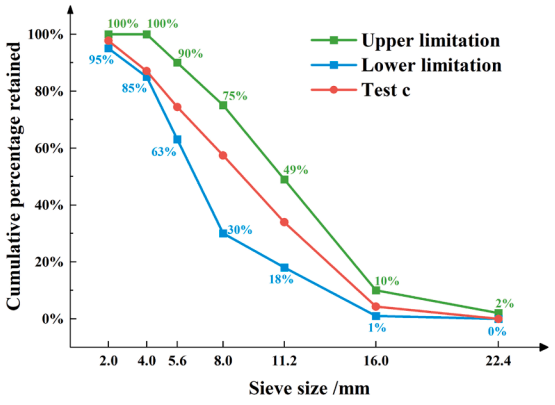

(c) Test C

Fig. 17. Comparison before and after optimization.

directly on a high-speed conveyor belt, achieving a processing rate of at least 50 tons per hour. This real-time capability fills a critical gap in the literature and provides essential scalability for deployment in modern concrete recycling facilities.

The proposed method incorporates several technical advancements over conventional approaches. First, we developed a customized watershed segmentation algorithm tailored to the highly irregular morphology of RCA particles, which ensures robust delineation of overlapping particles by leveraging both global topological and gradient-based information. Second, we implemented a linear programming-based PSD adjustment mechanism that intelligently corrects the measured distribution to meet European standard requirements—an approach not previously combined with real-time scanning. Third, we validated a practical, strip-based sampling strategy using a 20 mm-wide region located one-third from the top of the RCA pile. This area was experimentally confirmed to provide a representative PSD with RMSE values as low as 4.10 %, enabling efficient and accurate PSD estimation without full-surface scanning. This research is among the first to integrate real-time 3D scanning, watershed-based segmentation, and PSD optimization into a closed-loop system for RCA quality control under dynamic, high-throughput industrial conditions.

Recognizing that RCA sources significantly affect PSD outcomes underscores the necessity of integrating detailed source characterization into the quality assurance process, which is vital for reliably predicting aggregate performance and optimizing processing strategies. Future research should aim to systematically expand the variety of RCA sources investigated, thoroughly examining the specific influence of different demolition origins—including variations in building type, concrete quality, and demolition techniques—on PSD characteristics. By incorporating RCA source as a distinct parameter, it will be possible to establish a comprehensive comparative analysis, providing clearer insights into how source-specific factors influence PSD. Such research would greatly enhance our ability to predict and manage variability, thus optimizing aggregate processing, reducing uncertainty, and fostering broader application of recycled aggregates in sustainable construction practices.

While this study shows some clear benefits, it also acknowledges certain limitations that necessitate additional investigation. Although the current study focuses primarily on demonstrating a rapid assessment and optimization method for PSD in industrial settings, future work will include developing and integrating algorithms to identify and analyze deformed aggregates. Such algorithms are expected to enhance the robustness of the proposed system by accommodating irregular particle morphologies and further improving the accuracy of PSD measurement and optimization. Future research could beneficially explore the scalability of the proposed method, particularly its applicability across diverse aggregate types. Moreover, addressing the existing constraints in the algorithm's performance remains a crucial area for further refinement. Subsequent studies might productively focus on enhancing the algorithm's efficiency, extending the method's applicability to a broader range of conveyor systems, and strategically integrating this technology within other quality control frameworks to optimize overall process efficiency.

CRediT authorship contribution statement

Cheng Chang: Writing – original draft, Visualization, Validation, Software, Methodology, Investigation, Formal analysis, Data curation, Conceptualization. **Francesco Di Maio:** Writing – review & editing, Supervision, Project administration, Methodology, Funding acquisition, Conceptualization. **Rajeev Bheemireddy:** Software, Data curation. **Perry Posthoorn:** Software, Data curation. **Abraham T. Gebremariam:** Writing – review & editing, Resources. **Peter Rem:** Writing – review & editing, Supervision, Project administration, Methodology, Funding acquisition, Conceptualization.

Declaration of competing interest

The authors declare that they have no known competing financial interests or personal relationships that could have appeared to influence the work reported in this paper.

Acknowledgements

This work was supported by the European Union's Horizon 2020 funded Project " Innovative Circular Economy Based solutions demonstrating the Efficient Recovery of valuable material resources from the Generation of representative end-of-life building materials" (ICEBERG, grant agreement No. 869336).

Data availability

Data will be made available on request.

References

[1] E. Khoury, W. Ambrós, B. Cazacliu, C.H. Sampaio, S. Remond, Heterogeneity of recycled concrete aggregates, an intrinsic variability, Constr. Build. Mater. 175 (2018) 705–713, https://doi.org/10.1016/J.CONBUILDMAT.2018.04.163.
[2] A. Jayasuriya, M.P. Adams, M.J. Bandelt, Understanding variability in recycled aggregate concrete mechanical properties through numerical simulation and statistical evaluation, Constr. Build. Mater. 178 (2018) 301–312, https://doi.org/10.1016/J.CONBUILDMAT.2018.05.158.
[3] J. Pacheco, J. de Brito, C. Chastre, L. Evangelista, Experimental investigation on the variability of the main mechanical properties of concrete produced with coarse recycled concrete aggregates, Constr. Build. Mater. 201 (2019) 110–120, https://doi.org/10.1016/J.CONBUILDMAT.2018.12.200.
[4] M. Etxeberria, The suitability of concrete using recycled aggregates (RAs) for high-performance concrete, Adv. Constr. Demolition Waste Recycl.: Manag. Process. Environ. Assess. (2020) 253–284, https://doi.org/10.1016/B978-0-12-819055-5.00013-9.
[5] A. Lotfy, M. Al-Fayez, Performance evaluation of structural concrete using controlled quality coarse and fine recycled concrete aggregate, Cem. Concr. Compos. 61 (2015) 36–43, https://doi.org/10.1016/J.CEMCONCOMP.2015.02.009.
[6] S.C. Kou, C.S. Poon, Effect of the quality of parent concrete on the properties of high performance recycled aggregate concrete, Constr. Build. Mater. 77 (2015) 501–508, https://doi.org/10.1016/J.CONBUILDMAT.2014.12.035.
[7] D. Pedro, J. de Brito, L. Evangelista, Mechanical characterization of high performance concrete prepared with recycled aggregates and silica fume from precast industry, J. Clean. Prod. 164 (2017) 939–949, https://doi.org/10.1016/J.JCLEPRO.2017.06.249.
[8] C. Chang, F. Di Maio, P. Rem, A.T. Gebremariam, F. Mehari, H. Xia, Cluster-based identification algorithm for in-line recycled concrete aggregates characterization using laser-induced breakdown spectroscopy (LIBS), Resour. Conserv. Recycl. 185 (2022) 106507, https://doi.org/10.1016/J.RESCONREC.2022.106507.
[9] B. Wang, L. Yan, Q. Fu, B. Kasal, A comprehensive review on recycled aggregate and recycled aggregate concrete, Resour. Conserv. Recycl. 171 (2021) 105565, https://doi.org/10.1016/J.RESCONREC.2021.105565.
[10] H.K.A. Al-Bayati, P.K. Das, S.L. Tighe, H. Baaj, Evaluation of various treatment methods for enhancing the physical and morphological properties of coarse recycled concrete aggregate, Constr. Build. Mater. 112 (2016) 284–298, https://doi.org/10.1016/J.CONBUILDMAT.2016.02.176.
[11] L. Evangelista, M. Guedes, J. De Brito, A.C. Ferro, M.F. Pereira, Physical, chemical and mineralogical properties of fine recycled aggregates made from concrete waste, Constr. Build. Mater. 86 (2015) 178–188, https://doi.org/10.1016/J.CONBUILDMAT.2015.03.112.
[12] C. Chang, F. Di Maio, R. Bheemireddy, P. Posthoorn, A.T. Gebremariam, P. Rem, Rapid quality control for recycled coarse aggregates (RCA) streams: multi-sensor integration for advanced contaminant detection, Comput. Ind. 164 (2025) 104196, https://doi.org/10.1016/j.compind.2024.104196.
[13] C. Chang, F. Di Maio, R. Bheemireddy, P. Posthoorn, A.T. Gebremariam, P. Rem, Enhancing quality inspection efficiency and reliability of unscreened recycled coarse aggregates (RCA) streams using innovative mobile sensor-based technology, Dev. Built Environ. 21 (2025) 100611, https://doi.org/10.1016/J.DIBE.2025.100611.
[14] C. Chang, Quality assessment & monitoring of recycled coarse aggregates, 2025. https://doi.org/10.4233/uuid:ca80614c-747f-4ef8-95aa-78c0b193d261.
[15] M.S. Meddah, S. Zitouni, S. Belâabes, Effect of content and particle size distribution of coarse aggregate on the compressive strength of concrete, Constr. Build. Mater. 24 (2010) 505–512, https://doi.org/10.1016/J.CONBUILDMAT.2009.10.009.
[16] A.P.N. Siregar, M.I. Rafiq, M. Mulheron, Experimental investigation of the effects of aggregate size distribution on the fracture behaviour of high strength concrete, Constr. Build. Mater. 150 (2017) 252–259, https://doi.org/10.1016/J.CONBUILDMAT.2017.05.142.

[17] J. Wu, M. Feng, X. Mao, J. Xu, W. Zhang, X. Ni, G. Han, Particle size distribution of aggregate effects on mechanical and structural properties of cemented rockfill: experiments and modeling, Constr. Build. Mater. 193 (2018) 295–311, https://doi.org/10.1016/J.CONBUILDMAT.2018.10.208.
[18] S. Zong, C. Chang, P. Rem, A.T. Gebremariam, F. Di Maio, Y. Lu, Research on the influence of particle size distribution of high-quality recycled coarse aggregates on the mechanical properties of recycled concrete, Constr. Build. Mater. 465 (2025) 140253, https://doi.org/10.1016/J.CONBUILDMAT.2025.140253.
[19] M. Nedeljković, J. Visser, B. Šavija, S. Valcke, E. Schlangen, Use of fine recycled concrete aggregates in concrete: a critical review, J. Build. Eng. 38 (2021) 102196, https://doi.org/10.1016/J.JOBE.2021.102196.
[20] H. Yoshida, T. Yamamoto, Y. Mori, H. Masuda, K. Okazaki, H. Sugasawa, Particle size measurement of reference particle candidates and uncertainty region of count and mass based cumulative distribution, Adv. Powder. Technol. 25 (2014) 1748–1753, https://doi.org/10.1016/J.APT.2014.07.001.
[21] M.V.A. Florea, H.J.H. Brouwers, Properties of various size fractions of crushed concrete related to process conditions and re-use, Cem. Concr. Res. 52 (2013) 11–21, https://doi.org/10.1016/J.CEMCONRES.2013.05.005.
[22] C.R. Wu, Z.Q. Hong, J.L. Zhang, S.C. Kou, Pore size distribution and ITZ performance of mortars prepared with different bio-deposition approaches for the treatment of recycled concrete aggregate, Cem. Concr. Compos. 111 (2020) 103631, https://doi.org/10.1016/J.CEMCONCOMP.2020.103631.
[23] B. Mazhoud, T. Sedran, B. Cazacliu, A. Cothenet, J.M. Torrenti, Influence of residual mortar volume on the properties of recycled concrete aggregates, J. Build. Eng. 57 (2022) 104945, https://doi.org/10.1016/J.JOBE.2022.104945.
[24] B. Tanane, M.L. Bentaha, B. Dafflon, N. Moalla, Bridging the gap between Industry 4.0 and manufacturing SMEs: a framework for an end-to-end total manufacturing quality 4.0's implementation and adoption, J. Ind. Inf. Integr. 45 (2025) 100833, https://doi.org/10.1016/J.JII.2025.100833.
[25] L. Gao, D. Wang, Y. Miao, A review of two-dimensional image-based technologies for size and shape characterization of coarse-grained granular soils, Powder. Technol. 445 (2024) 120115, https://doi.org/10.1016/J.POWTEC.2024.120115.
[26] H. Sun, B. Fan, S.A. Memon, Z. Cen, X. Gao, B. Lin, B. Liu, D. Li, F. Xing, X. Zhang, 3D particle size distribution of inter-ground Portland limestone/slag cement from 2D observations: characterization and distribution evaluation, Constr. Build. Mater. 147 (2017) 550–557, https://doi.org/10.1016/J.CONBUILDMAT.2017.04.070.
[27] W. Wang, C. Li, X. Zhao, P. Song, J. Li, J. Zheng, S. Bu, X. Wang, An image-based method for evaluating changes in particle size and morphology distributions of aggregate materials after vibratory compaction test, Constr. Build. Mater. 430 (2024) 136483, https://doi.org/10.1016/J.CONBUILDMAT.2024.136483.
[28] S. Al-Thyabat, N.J. Miles, An improved estimation of size distribution from particle profile measurements, Powder. Technol. 166 (2006) 152–160, https://doi.org/10.1016/J.POWTEC.2006.05.008.
[29] M. Akashi, T. Otani, A. Shimosaka, Y. Shirakawa, J. Hidaka, Estimation of particle size distribution from cross-sectional particle diameter on the cutting plane, Adv. Powder. Technol. 21 (2010) 676–680, https://doi.org/10.1016/J.APT.2010.08.003.
[30] Y. Hu, J. Wang, X. Wang, Y. Sun, H. Yu, J. Zhang, Real-time evaluation of the blending uniformity of industrially produced gravelly soil based on Cond-YOLOv8-seg, J. Ind. Inf. Integr. 39 (2024) 100603, https://doi.org/10.1016/J.JII.2024.100603.
[31] S. Shrivastava, D. Deb, S. Bhattacharjee, Prediction of particle size distribution curves of dump materials using convolutional neural networks, Rock. Mech. Rock. Eng. 55 (2022) 471–479, https://doi.org/10.1007/S00603-021-02657-Y/FIGURES/7.
[32] X. Yang, T. Ren, L. Tan, Size distribution measurement of coal fragments using digital imaging processing, Measurement 160 (2020) 107867, https://doi.org/10.1016/J.MEASUREMENT.2020.107867.
[33] S. Tafesse, J.M.R. Fernlund, F. Bergholm, Digital sieving-Matlab based 3-D image analysis, Eng. Geol. 137–138 (2012) 74–84, https://doi.org/10.1016/J.ENGGEO.2012.04.001.
[34] S. Chatterjee, A. Bhattacherjee, B. Samanta, S.K. Pal, Image-based quality monitoring system of limestone ore grades, Comput. Ind. 61 (2010) 391–408, https://doi.org/10.1016/J.COMPIND.2009.10.003.
[35] J. Tessier, C. Duchesne, G. Bartolacci, A machine vision approach to on-line estimation of run-of-mine ore composition on conveyor belts, Min. Eng. 20 (2007) 1129–1144, https://doi.org/10.1016/J.MINENG.2007.04.009.
[36] F. Bai, M. Fan, H. Yang, L. Dong, Image segmentation method for coal particle size distribution analysis, Particuology 56 (2021) 163–170, https://doi.org/10.1016/J.PARTIC.2020.10.002.
[37] E. Hamzeloo, M. Massinaei, N. Mehrshad, Estimation of particle size distribution on an industrial conveyor belt using image analysis and neural networks, Powder. Technol. 261 (2014) 185–190, https://doi.org/10.1016/J.POWTEC.2014.04.038.
[38] X. Wu, X.Y. Liu, W. Sun, C.G. Mao, C. Yu, An image-based method for online measurement of the size distribution of iron green pellets using dual morphological reconstruction and circle-scan, Powder. Technol. 347 (2019) 186–198, https://doi.org/10.1016/J.POWTEC.2019.03.007.
[39] M. Kistner, G.T. Jemwa, C. Aldrich, Monitoring of mineral processing systems by using textural image analysis, Min. Eng. 52 (2013) 169–177, https://doi.org/10.1016/J.MINENG.2013.05.022.
[40] Z. Zhang, J. Yang, L. Ding, Y. Zhao, An improved estimation of coal particle mass using image analysis, Powder. Technol. 229 (2012) 178–184, https://doi.org/10.1016/J.POWTEC.2012.06.027.
[41] T. Bamford, K. Esmaeili, A.P. Schoellig, A deep learning approach for rock fragmentation analysis, Int. J. Rock Mech. Min. Sci. 145 (2021) 104839, https://doi.org/10.1016/J.IJRMMS.2021.104839.
[42] H. Yaghoobi, H. Mansouri, M.A. Ebrahimi Farsangi, H. Nezamabadi-Pour, Determining the fragmented rock size distribution using textural feature extraction of images, Powder. Technol. 342 (2019) 630–641, https://doi.org/10.1016/J.POWTEC.2018.10.006.
[43] L.E. Olivier, M.G. Maritz, I.K. Craig, Estimating ore particle size distribution using a deep convolutional neural network, IFAC-Pap. 53 (2020) 12038–12043, https://doi.org/10.1016/J.IFACOL.2020.12.740.
[44] I.C. Engin, N.H. Maerz, Size distribution analysis of aggregates using LiDAR scan data and an alternate algorithm, Measurement 143 (2019) 136–143, https://doi.org/10.1016/J.MEASUREMENT.2019.04.071.
[45] Z. Zhang, Y. Liu, Q. Hu, Z. Zhang, L. Wang, X. Liu, X. Xia, Multi-information online detection of coal quality based on machine vision, Powder. Technol. 374 (2020) 250–262, https://doi.org/10.1016/J.POWTEC.2020.07.040.
[46] F. Khalifa, M. Marzouk, Integrated blockchain and Digital Twin framework for sustainable building energy management, J. Ind. Inf. Integr. 43 (2025) 100747, https://doi.org/10.1016/J.JII.2024.100747.
[47] I. Petri, Y. Rezgui, A. Ghoroghi, A. Alzahrani, Digital twins for performance management in the built environment, J. Ind. Inf. Integr. 33 (2023) 100445, https://doi.org/10.1016/J.JII.2023.100445.
[48] S. Perera, S. Nanayakkara, M.N.N. Rodrigo, S. Senaratne, R. Weinand, Blockchain technology: is it hype or real in the construction industry? J. Ind. Inf. Integr. 17 (2020) 100125 https://doi.org/10.1016/J.JII.2020.100125.
[49] S. Ahmadisheykhsarmast, S. Aminbakhsh, R. Sonmez, F. Uysal, A transformative solution for construction safety: blockchain-based system for accident information management, J. Ind. Inf. Integr. 35 (2023) 100491, https://doi.org/10.1016/J.JII.2023.100491.
[50] Ö.F. Görçün, A. Saha, F. Ecer, Evaluation of crawler cranes for large-scale construction and infrastructure projects: an intuitionistic fuzzy consensus-based approach, J. Ind. Inf. Integr. 44 (2025) 100784, https://doi.org/10.1016/J.JII.2025.100784.
[51] C. Wang, L. han Song, Z. Yuan, J. sheng Fan, State-of-the-art AI-based computational analysis in civil engineering, J. Ind. Inf. Integr. 33 (2023) 100470, https://doi.org/10.1016/J.JII.2023.100470.
[52] R. Mohanraj, B.K. Vaishnavi, Data enabling technology in digital twin and its frameworks in different industrial applications, J. Ind. Inf. Integr. 44 (2025) 100793, https://doi.org/10.1016/J.JII.2025.100793.
[53] C. Semeraro, M. Lezoche, H. Panetto, M. Dassisti, Data-driven invariant modelling patterns for digital twin design, J. Ind. Inf. Integr. 31 (2023) 100424, https://doi.org/10.1016/J.JII.2022.100424.
[54] S. Yoon, Y. Choi, J. Koo, In situ virtual sensors in building digital twins: framework and methodology, J. Ind. Inf. Integr. 36 (2023) 100532, https://doi.org/10.1016/J.JII.2023.100532.
[55] S. Perera, X. Jin, P. Das, K. Gunasekara, M. Samaratunga, A strategic framework for digital maturity of design and construction through a systematic review and application, J. Ind. Inf. Integr. 31 (2023) 100413, https://doi.org/10.1016/J.JII.2022.100413.
[56] M.K. Chenchu, K. Ruikar, K.N. Jha, Structural equation modeling of data usage factors in the construction sector: a comprehensive validation of micro level data usage factors, J. Ind. Inf. Integr. 45 (2025) 100828, https://doi.org/10.1016/J.JII.2025.100828.
[57] Z.M. Bia, L. Wang, Advances in 3D data acquisition and processing for industrial applications, Robot. Comput. Integr. Manuf. 26 (2010) 403–413, https://doi.org/10.1016/J.RCIM.2010.03.003.
[58] M. Bilušić, L. Olivari, Assessment of process chain suitability of the optical 3D measuring system by using influencing factors for measurement uncertainty, J. Ind. Inf. Integr. 41 (2024) 100654, https://doi.org/10.1016/J.JII.2024.100654.
[59] M. Sommer, J. Stjepandić, S. Stobrawa, M. von Soden, Automated generation of digital twin for a built environment using scan and object detection as input for production planning, J. Ind. Inf. Integr. 33 (2023) 100462, https://doi.org/10.1016/J.JII.2023.100462.
[60] C. Emmer, T.M. Hofmann, T. Schmied, J. Stjepandić, M. Strietzel, A neutral approach for interoperability in the field of 3D measurement data management, J. Ind. Inf. Integr. 12 (2018) 47–56, https://doi.org/10.1016/J.JII.2018.01.006.
[61] M.J. Thurley, Automated online measurement of limestone particle size distributions using 3D range data, J. Process. Control 21 (2011) 254–262, https://doi.org/10.1016/J.JPROCONT.2010.11.011.
[62] E. Bottani, R. Montanari, A. Volpi, L. Tebaldi, Statistical process control of assembly lines in manufacturing, J. Ind. Inf. Integr. 32 (2023) 100435, https://doi.org/10.1016/J.JII.2023.100435.
[63] F.J. Galdames, C.A. Perez, P.A. Estévez, M. Adams, Classification of rock lithology by laser range 3D and color images, Int J Min. Process 160 (2017) 47–57, https://doi.org/10.1016/J.MINPRO.2017.01.008.
[64] K. Souaïbou Hawaou, V.C. Kamla, S. Yassa, O. Romain, J.E. Ndamlabin Mboula, L. Bitjoka, Industry 4.0 and industrial workflow scheduling: a survey, J. Ind. Inf. Integr. 38 (2024) 100546, https://doi.org/10.1016/J.JII.2023.100546.
[65] A. Schlemitz, V. Mezhuyev, Approaches for data collection and process standardization in smart manufacturing: systematic literature review, J. Ind. Inf. Integr. 38 (2024) 100578, https://doi.org/10.1016/J.JII.2024.100578.
[66] S.P. Mishra, A. Kamaraj, V. Rajinikanth, M.R. Rahul, A computer vision-based approach for identification of non-metallic inclusions in the steel industry, J. Ind. Inf. Integr. (2025) 100860, https://doi.org/10.1016/J.JII.2025.100860.

[67] M. Mazzoleni, Design of supervision solutions for industrial equipment: schemes, tools and guidelines for the user, J. Ind. Inf. Integr. 41 (2024) 100667, https://doi.org/10.1016/J.JII.2024.100667.
[68] H. Ali, R. Safdar, M.H. Rasool, H. Anjum, Y. Zhou, Y. Yao, L. Yao, F. Gao, Advance industrial monitoring of physio-chemical processes using novel integrated machine learning approach, J. Ind. Inf. Integr. 42 (2024) 100709, https://doi.org/10.1016/J.JII.2024.100709.
[69] M. Borhani, G.S. Gaba, J. Basaez, I. Avgouleas, A. Gurtov, A critical analysis of the industrial device scanners' potentials, risks, and preventives, J. Ind. Inf. Integr. 41 (2024) 100623, https://doi.org/10.1016/J.JII.2024.100623.
[70] J. Singh, A. Singh, H. Singh, P. Doyon-Poulin, Implementation and evaluation of a smart machine monitoring system under Industry 4.0 concept, J. Ind. Inf. Integr. 43 (2025) 100746, https://doi.org/10.1016/J.JII.2024.100746.
[71] A.T. Gebremariam, F. Di Maio, A. Vahidi, P. Rem, Innovative technologies for recycling end-of-life concrete waste in the built environment, Resour. Conserv. Recycl. 163 (2020), https://doi.org/10.1016/j.resconrec.2020.104911.
[72] J.P. Wilson, J.C. Gallant, Terrain Analysis: Principles and Applications, John Wiley & Sons, 2000.
[73] J.F. O'Callaghan, D.M. Mark, The extraction of drainage networks from digital elevation data, Comput. Vis. Graph. Image Process. 28 (1984) 323–344, https://doi.org/10.1016/S0734-189X(84)80011-0.
[74] P. Steer, L. Guerit, D. Lague, A. Crave, A. Gourdon, Size, shape and orientation matter: fast and semi-automatic measurement of grain geometries from 3D point clouds, Earth Surf. Dyn. 10 (2022) 1211–1232, https://doi.org/10.5194/esurf-10-1211-2022.
[75] J. Braun, S.D. Willett, A very efficient O(n), implicit and parallel method to solve the stream power equation governing fluvial incision and landscape evolution, Geomorphology 180–181 (2013) 170–179, https://doi.org/10.1016/J.GEOMORPH.2012.10.008.
[76] B. Standard, Aggregates for concrete, BS EN 12620 (2002).